

Dear author,

Please note that changes made in the online proofing system will be added to the article before publication but are not reflected in this PDF.

We also ask that this file not be used for submitting corrections.



Contents lists available at ScienceDirect

Journal of the Mechanics and Physics of Solids

journal homepage: www.elsevier.com/locate/jmps

The complexity of non-Schmid behavior in the CuZnAl shape memory alloy

Q1 S. Alkan, A. Ojha, H. Sehitoglu*

Department of Mechanical Science and Engineering, University of Illinois at Urbana-Champaign, 1206W. Green Street, Urbana, IL 61801, USA

ARTICLE INFO

Article history:

Received 1 September 2017
 Revised 20 February 2018
 Accepted 26 February 2018
 Available online xxx

ABSTRACT

The paper addresses one of the most important yet overlooked phenomenon in shape memory research- the plastic slip response. We show that the slip response is highly crystal orientation dependent and we demonstrate the precise reasons behind such complex response. The fractional dislocations on $<111> \{112\}$ or $<111> \{011\}$ systems can be activated depending on the sample orientation and solutions are derived for the variations in disregistrys and dislocation core spreadings. This leads to the calculation of critical resolved shear stress in close agreement with experimental trends. The results show considerable dependence of the flow behavior on the non-Schmid stress components and the proposed yield criterion captures the role of stress tensor components.

© 2018 Published by Elsevier Ltd.

1 1. Introduction

2 The plastic deformation of shape memory alloys remains one of the most intriguing topics of research because the
 3 yielding behavior does not follow the well-known Schmid law that has been primarily developed for face centered cubic (fcc) and hexagonal close packed (hcp) metals ([Schmid and Boas, 1950](#)). Most shape memory alloys have an austenitic cubic structure such as a B2 or L2₁, (i.e. ordered lattices) and undergo slip in {011} and/or {112} planes ([Otsuka and Wayman, 1998](#); [Chowdhury and Sehitoglu, 2016](#)). A noteworthy observation is that because the dislocation core spreading occurs on conjugate slip planes, the description of the plastic flow must account for non-glide stress components ([Alkan and Sehitoglu, 2017](#)). Consequently, the description of yielding for plasticity at the crystal lattice level must embrace a form that departs from the well-known Schmid law. Recent research results and simulation efforts have focused on Fe₃Al ([Alkan and Sehitoglu, 2017](#)) and NiTi ([Alkan et al., 2017](#); [Alkan and Sehitoglu, 2017](#)), and for the first time a new yield criterion was proposed accounting for non-glide stresses for these two ordered shape memory alloys at the crystal level. Before expounding on the details of the non-Schmid behavior in shape memory alloys, we provide an overview of the flow behavior in body centered cubic (bcc) materials.

4 Dating back to the early experiments of [Taylor \(1928\)](#) the complicated plastic deformation behavior of bcc metals and
 5 alloys has been of interest for numerous researchers ([Vitek, 1974](#); [Basinski et al., 1981](#); [Duesbery, 1984](#); [Duesbery, 1984](#);
 6 [Yamaguchi and Umakoshi, 1983](#); [Sherwood et al., 1967](#); [Gröger et al., 2008](#); [Gröger et al., 2008](#); [Lin et al., 2012](#)). With the
 7 emergence of the atomistic scale simulation capabilities in the late sixties ([Chang, 1967](#); [Vitek, 1968](#); [Duesbery et al., 1973](#);
 8 [Suzuki, 1968](#)), the dislocation core structure and short range interatomic forces are determined to be responsible for this
 9 experimentally observed complexity. On the other hand, the studies in the last three decades have undoubtedly shown that

* Corresponding author.

E-mail address: huseyin@illinois.edu (H. Sehitoglu).

the screw dislocations inside the bcc-based ordered lattice structures generally exhibit strong deviations from the critical resolved shear stress (CRSS) law (also known as Schmid Law (Schmid and Boas, 1950)), especially at low temperatures (Christian, 1983; Vitek, 1985). Recent experimental work and atomistic calculations report that shape memory alloys show pronounced deviations from Schmid Law owing to the strongly anisotropic nature of the interatomic forces persisting at finite temperatures (Alkan and Sehitoglu, 2017; Alkan et al., 2017; Hu et al., 2006). As Cu based shape memory alloys are finding more application fields owing to their cheaper cost, considerable transformation strain and high thermal/electrical conductivities (Otsuka and Wayman, 1998.; Sutou et al., 2008.; Wayman, 1980.; Gautier and Patoor, 1997.; Wu, 1990); in this work, we interrogated on the plastic deformation characteristics of L₂₁ ordered ternary CuZnAl (21.6 at. % Zn-13.15 at. % Al) alloy (Romero et al., 1988), briefly denoted as CuZnAl hereinafter, within the framework of *ab-initio* and continuum scale calculations.

In contrast with the close packed pure metals in which the slip motion is dictated by a unique CRSS value along the densest atomic direction - except the pyramidal and prismatic glide in hcp metals (Vitek, 1985), the glide resistance in bcc based structures exhibit strong interplay with the applied stress state in both pure metals and alloys (Duesbery and Vitek, 1998; Vitek and Paidar, 2008). This interaction leads to the non-unique CRSS values which are dependent on the external stress tensor. Complying with this hypothesis, earlier literature on CuZnAl addresses that significant CRSS differentials can be observed as a function of the single crystal orientation under uniaxial loading (Romero et al., 1988). The plastic deformation of CuZnAl is accommodated by the glide of super-lattice dislocations of a {111} type tending to glide on {110} and {112} planes (a is the lattice constant of CuZnAl 5.828 Å (Wu et al., 2015)) (Jara et al., 1985). Furthermore, this super-lattice dislocation dissociates into the four partial dislocations of each having $a/4$ {111} Burgers vector. The partials are joint by the Nearest Neighbor (NN) and Next Nearest Neighbor (NNN) Antiphase boundary (APB) faults which are formed due to the change in NN and NNN lattice sites of L₂₁ ordered crystal structure.

Previous studies in the literature indicate that the core structure of the screw character partials in L₂₁ ordered lattices exhibit non-planar extension on {110} and/or {112} family planes within the glide zone of {111} (Yamaguchi and Umakoshi, 1983; Duesbery and Richardson, 1991). The distribution of slip inside the non-planar core structure is surmised to exhibit strong interplay with the external stress tensor and therefore results in deviations from the Schmid Law complying with the experimental observations (Romero et al., 1988). In the sequel, we would like to develop a quantitative understanding to predict the non-unique CRSS values in CuZnAl. To that end, we probed the interaction between the screw dislocation core shape and the external stress state within the framework of a multiscale (atomistic-continuum) slip energetics formulation. To accomplish this task, we generated the GSFE profiles along the {111} {110} and {111} {112} glide systems via *ab-initio* calculations. Adopting these GSFE profiles into the total energy formulation of a dissociated a {111} super-lattice screw dislocation, we constructed a solution algorithm contingent on the constrained minimization of the total energy expression. The calculations employ the anisotropic dislocation theory (Steeds, 1973; Hirth and Lothe, 1968) and encompasses the contribution of both four $a/4$ {111} partials and the fractional dislocations inside the leading partial core on the CRSS values for slip. Within these efforts, the non-planar core structure of the leading partial plays a key role. To that end, the possible leading core configurations under external stress are also incorporated into the model to capture the core shape in response to the different external stress components. Notably, this theoretical analysis helps pave the way for a deeper comprehension of the interaction between the core configurations and the CRSS levels exhibiting non-Schmid behavior.

Although a rich body of literature surrounds the atomistic-scale core behavior in bcc-based lattice structures; yet much remains to be incorporated into the conventional crystal plasticity calculations to embrace the deviations from the Schmid law. The contribution of the non-glide stress components to the plastic yielding has been addressed for pure bcc metals only within a limited number of studies (Gröger et al., 2008; Patra et al., 2014; Lim et al., 2013; Dao and Asaro, 1993) in spirit of the framework by Qin and Bassani (1992). More recently, the current authors have proposed a generalized yield criterion accounting for the contribution of non-glide stress components (either shear or normal character) to the slip initiation in DO₃ ordered Fe₃Al and B2 ordered NiTi alloys (Alkan and Sehitoglu, 2017; Alkan et al., 2017; Alkan and Sehitoglu, 2017). The resulting theoretical predictions exhibit close agreement with the experimental behavior emphasizing the pronounced contribution of the non-glide stresses upon the CRSS levels in ordered shape memory alloys. As a forward step, in this work, we propose a generalized yield criterion based on the theoretical evaluation of the deviatoric stress components corresponding to the glide of a {111} super-lattice dislocation in CuZnAl. The resulting theoretical yield surface accomplishes to bridge the atomic scale dislocation core configurations to the macroscopic plastic yield behavior.

In summary, considering the intricate nature of the dislocation mediated slip in CuZnAl; we aim to quantify the slip energetics and develop a theoretical model to predict CRSS values. The model focuses on the stability of the total energy associated with a {111} super-dislocation in conjunction with the non-planar core shape of the leading partial. The predicted values are shown to be in close agreement with the systematic experimental measurements presented in the earlier literature (Romero et al., 1988). A discussion on the possible extensions of the proposed plastic glide model for the cyclic and superelastic behavior is also provided.

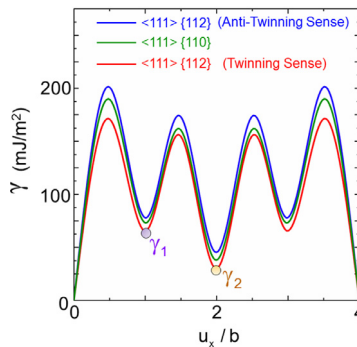


Fig. 1. Shows the generalized stacking fault energy (GSFE) curves along $\langle 111 \rangle \{110\}$ and $\langle 111 \rangle \{112\}$ slip systems considering the intrinsic asymmetry along the twinning and anti-twinning directions. The disregistry displacement u_x varies between 0 to $a |\langle 111 \rangle|$. The local minima γ_1 and γ_2 show the stable NNAPB and NNNAPB fault energy levels.

Table 1

Tabulation of the NNAPB and NNNAPB energy values, i.e. γ_1 and γ_2 , respectively, extracted from the GSFE curves of $\langle 111 \rangle \{112\}$ slip system along the twinning and the anti-twinning directions and $\langle 111 \rangle \{110\}$ system. The separation distances between the partials under zero external stress, i.e. d_1 and d_2 , are also included. It is to be noted that d_1 and d_2 values on $\{112\}$ plane are calculated based on the average γ_1 and γ_2 values of the twinning and the anti-twinning directions.

NNAPB $\gamma_1 \langle 111 \rangle \{112\}$ Twinning Sense (mJ/m ²)	61
NNNAPB $\gamma_2 \langle 111 \rangle \{112\}$ Twinning Sense (mJ/m ²)	26
NNAPB $\gamma_1 \langle 111 \rangle \{112\}$ Anti-Twinning Sense (mJ/m ²)	77
NNNAPB $\gamma_2 \langle 111 \rangle \{112\}$ Anti-Twinning Sense (mJ/m ²)	35
NNAPB $\gamma_1 \langle 111 \rangle \{110\}$ (mJ/m ²)	70
NNNAPB $\gamma_2 \langle 111 \rangle \{110\}$ (mJ/m ²)	31
$d_1 \langle 110 \rangle$ (nm)	2.6
$d_2 \langle 110 \rangle$ (nm)	13.40
$d_1 \langle 112 \rangle$ (nm) (average)	2.7
$d_2 \langle 112 \rangle$ (nm) (average)	13.45

75 2. Methods and theoretical background

76 2.1. Construction of generalized stacking fault energy (GSFE) curves

77 The uniaxial tension/compression experiments of Romero et al. (1988) conducted within a wide range of single crystal
 78 orientations along with the Transmission Electron Microscope (TEM) images address the single or combined activation of
 79 $\langle 111 \rangle \{112\}$, $\langle 111 \rangle \{110\}$ slip systems (Romero et al., 1988; Jara et al., 1985). Based on this experimental evidence, we gen-
 80 erated the GSFE curves of CuZnAl alloy along the $\langle 111 \rangle \{112\}$ and $\langle 111 \rangle \{110\}$ glide systems by utilizing Vienna ab-initio
 81 Simulation Package (VASP) with the projector augmented wave method and generalized gradient approximation (Kresse and
 82 Furthmüller, 1996; Kresse and Hafner, 1993). In the simulation procedure, a $2 \times 7 \times 2$ supercell with 112 atoms is constructed
 83 in a L_1 lattice structure. The simulations are performed using $12 \times 5 \times 12$ k points for Brillouin zone integration within the
 84 framework of Monkhorst Pack meshing procedure. The resulting energy values are ensured to converge within 10^{-5} eV/atom
 85 tolerance using conjugate gradient algorithm. An energy cut-off value of 360 eV with plane wave basis set was implemented
 86 in the simulations. The atoms are allowed to relax along all but the $\langle 111 \rangle$ direction. The resulting GSFE curves along the
 87 $\langle 111 \rangle \{110\}$ and $\langle 111 \rangle \{112\}$ systems- considering the intrinsic asymmetry for the twining and anti-twinning senses- are
 88 shown in Fig. 1.

89 As can be seen in Fig. 1, the dissociated configuration of a $\langle 111 \rangle$ dislocation observed in the earlier TEM studies is
 90 reflected in the energy profiles of slip along both $\langle 111 \rangle \{112\}$ and $\langle 111 \rangle \{110\}$ systems by the four local maxima (Jara et al.,
 91 1985; Sade et al., 1987). These local maximum energy barrier values are separated by the stable local minima located at
 92 the disregistry levels of $u_x = (n/4) \langle 111 \rangle$ where $n = 1, 2, 3$. For $n = 1, 3$; the local energy minima correspond to NNAPB energy
 93 levels, i.e. shown as γ_1 in Fig. 1(a); meanwhile NNNAPB energy level corresponds to the local minimum at $n = 2$ which is
 94 denoted as γ_2 . The numerical values of these energy levels calculated via the *ab-initio* calculations are tabulated in Table 1.
 95 These APB energy levels are of paramount importance in governing the core configuration of super-lattice partials, with
 96 equal Burgers vector of $\mathbf{b} = a/4 \langle 111 \rangle$ ($b = |\mathbf{b}|$), via exerting restoring forces on them.

97 The equilibrium separation distances d_1 and d_2 between the screw partials in externally stress free configuration, as
 98 illustrated in Fig. 2, are evaluated by the balance of the repulsive dislocation interaction forces with the restoring forces
 99 originating from the NNAPB and NNNAPB faults. The stable APB energy values of γ_1 and γ_2 are related to the distances

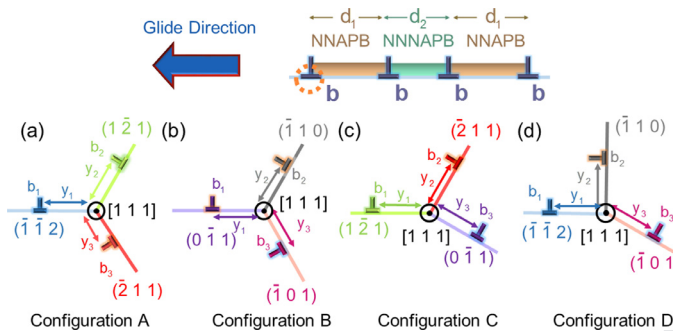


Fig. 2. Shows the possible core configurations of the a/4 <111> leading partial in CuZnAl.

of d_1 and d_2 as (Crawford et al., 1973):

$$\gamma_1 = \frac{K_s b^2}{2\pi} \left\{ \frac{1}{d_1} + \frac{1}{d_1 + d_2} + \frac{1}{2d_1 + d_2} \right\} \quad (1)$$

$$\gamma_2 = \frac{K_s b^2}{2\pi} \left\{ \frac{2}{d_1 + d_2} + \frac{1}{2d_1 + d_2} + \frac{1}{d_2} \right\} \quad (2)$$

The resulting d_1 and d_2 values from the simultaneous solution of the expressions in Eqs. (1) and (2) are tabulated in Table 1 for both {110} and {112} planes. K_s , appearing in Eqs. (1) and (2), is an anisotropic coefficient dependent on the lattice structure and is equal to 84 GPa (Steeds, 1973; Lothe, 1992; Foreman, 1955). The resulting value of d_1 is in close agreement with the experimental measurement of 3 nm (Romero et al., 1988) justifying the GSFE profile in Fig. 1 generated from the *ab-initio* calculations.

2.2. Non-planar core structure of a/4 <111> partials

The earlier atomistic scale calculations focusing on the dislocation core structure in bcc lattices, have a consensus that the core displacements of a/2 <111> screw dislocations mainly extend on {110} planes and no metastable stacking faults are present on the generated GSFE curves along the glide systems (Vitek, 1974; Gröger et al., 2008; Duesbery and Vitek, 1998; Frederiksen and Jacobsen, 2003; Duesbery, 1989). In externally stress-free configuration, a/2 [111] screw dislocation core in a bcc lattice has been evaluated to exhibit a threefold symmetry (with core spreading on {−101}, {0-11} and {−110} planes) for the pair (Vitek, 1974.; Vitek et al., 1970) and the Embedded Atom Method [Duesbery and Vitek, 1998; Wang et al., 2001] potentials with two degenerate energetically equivalent structures which are not invariant to {−101} diad symmetry. On the other hand, recent calculations based on the bond order potentials and first-principles calculations demonstrate a core possessing three-fold symmetry with additional {−101} diad symmetry operation for a/2 [111] screw dislocations leading to a non-degenerate structure (Gröger et al., 2008; Woodward and Rao, 2001) (For a review (Vitek and Paidar, 2008)). Generally, within the presence of external stress, the core spreading in a bcc lattice is cast into a more complicated shape which breaks the threefold symmetry along the <111> glide zone.

Extending the discussion to the ordered structures, i.e. B2, DO₃ and L₂1, points out a similar behavior for the screw core to that of the parent bcc lattice only with subtle variations. As a distinguishing point, in these alloy crystallite, the non-planar core structure has the tendency to prevent the overlap with the APB faults to minimize its energy (Duesbery and Richardson, 1991). For L₂1 ordered CuZnAl, the core structure may favor spreading on a combination of {112} and {110} planes depending on the slip energetics and the dislocation formation energy. Furthermore, the external stress tensor is also surmised to play a decisive role in the core spreading. On mechanical grounds, the configuration of the leading partial of a/4 <111> Burgers vector is of paramount importance to identify the CRSS required to pinpoint the slip initiation in CuZnAl. To that end, Fig. 2 summarizes the four possible leading core configurations for the particular case of a/4 [111] leading partial with the corresponding conjugate planes.

Among the core configurations illustrated in Fig. 2, configuration A favors the core spreading on the conjugate {112} family planes in the <111> glide zone. Two (one) of these conjugate planes promote glide in twinning (anti-twinning) sense. In configuration B, the core structure is spread on the conjugate {110} planes. The other possible configurations C and D, consist of a core which spreads on a combination of {112} and {110} planes. At this point, it is important to emphasize that the glide resistance in twinning sense on <111> {112} system is intrinsically lower than the anti-twinning sense. The departure from symmetry in the glide resistance along <111> {112} system originates from the symmetry group of bcc-based structures and is also reflected in the GSFE curves generated in Fig. 1.

Inside the core of each superpartial, the net a/4 <111> Burgers vector is distributed as of disregistry displacements, parallel to <111>, on the conjugate {110} and/or {112} planes (Yamaguchi and Umakoshi, 1983). An example of the non-planar core disregistry distributions, denoted as f_i ($i=1,2,3$), for configuration A of Fig. 2(a) is illustrated in Fig. 3(a). It should be noted

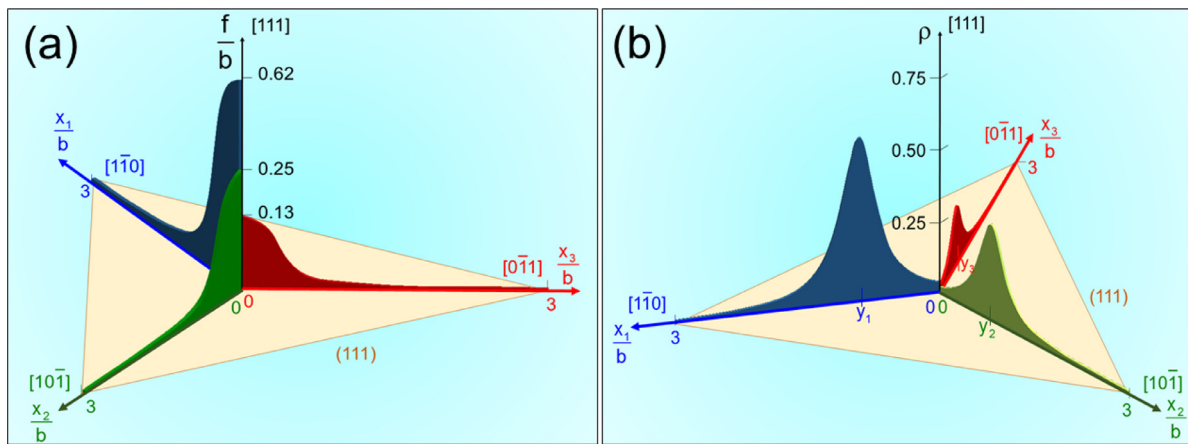


Fig. 3. (a) Illustrates a non-planar core configuration extending on $(\bar{1}\bar{1}2)$, $(\bar{2}11)$ and $(1\bar{2}1)$ planes. The resultant disregistry of the distributions f_i on each plane correspond to the partial dislocation Burgers vector b . (b) shows the infinitesimal dislocation density ρ_i which is determined based on the spatial gradient of f_i field on each plane. The geometric center of ρ_i , i.e. y_i , indicates the position of the fractional dislocations with the Burgers vector of $b_i = \max(f_i)$.

that the resultant of these slip distributions on the three conjugate planes sum up to b at the dislocation line center which corresponds to $x_i = 0$. The characteristic features of the f_i distribution will be further interrogated on mathematical grounds in the subsequent section.

In general, the disregistry displacements inside the non-planar core are identified as generalized stacking faults and do not correspond to a local minimum on the GSFE curve. To that end, these faults exhibit a different character from the partial dislocations which are separated by the stable stacking faults with a constant prescribed slip vectors, i.e. of either NNAPB or NNNAPB faults (Duesbery et al., 1973). Following the nomenclature of the earlier literature, the resultant of these disregistry displacements on each conjugate plane inside the core is denoted as the fractional dislocations (or fractionals) as shown in Fig. 2 (Vítek and Kroupa, 1969). The positions of the fractional dislocations, y_i , correspond to the geometric center of the infinitesimal-continuous dislocation density of ρ_i (Eshelby, 1949). From a mathematical perspective, ρ_i corresponds to the spatial derivative of f_i distribution (with respect to x_i coordinate). The Burgers vector of each fractional dislocation is denoted as b_i -shown in Fig. 2- and equal to the value of f_i at the dislocation line center -see Fig. 3(a).

2.3. Modelling the initiation of glide motion for the leading partial

To initiate the glide motion of the leading partial in CuZnAl under external stress, the fractionals change their positions and the core structure is said to transform from a sessile to a glissile configuration analogous to the $a/2 \langle 111 \rangle$ dislocation core structure in a pure bcc metal (Kroupa and Vítek, 1967). The positions of the fractionals are highly dependent on the external stress tensor to sustain equilibrium until the resolved shear stress acting on the most favorable slip system reaches a critical value, i.e. CRSS. Beyond this critical stress level, the fractional dislocation subjected to the highest glide force translates by multiple lattice spacings initiating plastic slip. Throughout this section, we will elaborate on developing a mathematical framework which can describe the slip initiation bridging external stress tensor with the core configuration.

Determination of the theoretical CRSS levels requires to incorporate the slip geometry into the total energy expression, E_{tot} . This formulation incorporates both long-range elastic and short-range misfit energy terms as well as the work done by the external stress components on the dissociated a $\langle 111 \rangle$ dislocation configuration. To that end, the external stress tensor σ applied on the sample should be described with respect to the dislocation coordinate frame. This task is accomplished by transforming the σ tensor from the sample frame $X_1 - X_2 - X_3$ to the dislocation frame $x_1 - x_2 - x_3$. The base vectors of these two orthonormal coordinate systems are denoted as $E_1 - E_2 - E_3$ and $e_1 - e_2 - e_3$ respectively. As illustrated in Fig. 4, these vectors are chosen on purpose in both coordinate frames. Meanwhile, E_2 coincides with the outwards normal of the surface on which the uniaxial loading is applied; the vectors e_2 and e_3 are chosen to be parallel to the active glide plane normal and its Burgers vector respectively. The transformation of the coordinates from the sample to the dislocation frame is accomplished via the orthogonal matrix Q_{ij} which is described as $Q_{ij} = e_i \cdot E_j$ where $i,j = 1,2,3$ (\bullet is the dot product operator). Following the second order tensor transformation rules, the external stress tensor is transformed to the dislocation coordinate frame, Σ , as in Eq. (3) where the summation convention is implied.

$$\Sigma_{ij} = Q_{ik} Q_{jm} \sigma_{km} \quad (i, j, k, m = 1, 2, 3) \quad (3)$$

Similarly, the transformation of the coordinates from the cubic crystal coordinate frame to the sample frame is accomplished by the orthogonal matrix R and its components are defined as $R_{ij} = \lambda_i \cdot E_j$ where λ_i are the unit base vectors of cubic crystal frame in Fig. 4.

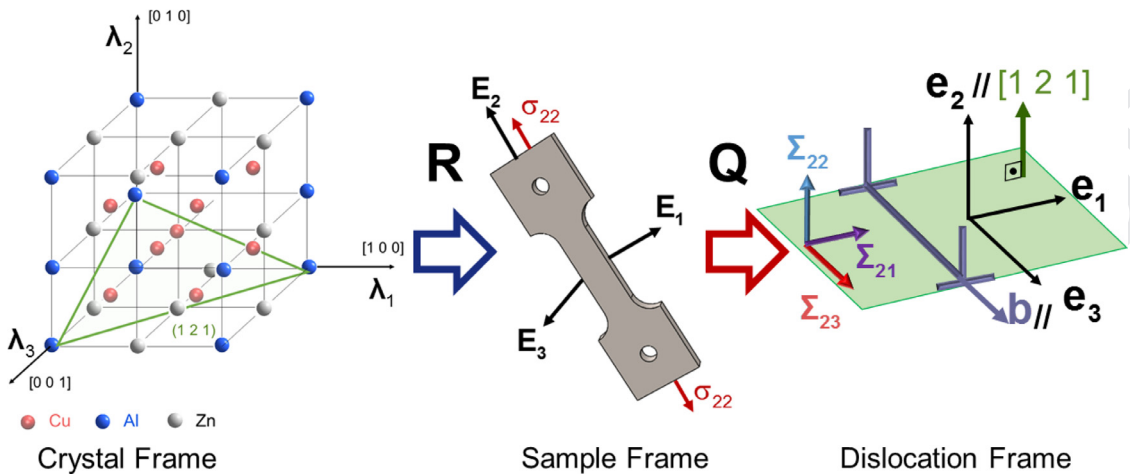


Fig. 4. Illustrates the cubic crystal frame [100]-[010]-[001], sample frame i.e. $X_1 - X_2 - X_3$ (with the base vectors of $E_1 - E_2 - E_3$) and the dislocation frame i.e. $x_1 - x_2 - x_3$ (with the base vectors of $e_1 - e_2 - e_3$). As can be seen, the coordinate transformation matrices R and Q can be used to transform the corresponding coordinates between the cubic, the sample and the dislocation frames.

In order to establish a solution scheme, E_{tot} , is constructed explicitly as the equilibrium of the system corresponds to the minimum total energy configuration, i.e. $\min.(E_{tot})$, whether an external stress field is present or not. Following this step, we delineated an energy minimization algorithm to find the updated positions of the leading partial- core fractionals under increasing loading intensity. In this proposed scheme, CRSS level corresponds to the glide shear stress, i.e. Σ_{23} , beyond which the matrix of second order partial derivatives (Hessian matrix) of E_{tot} function has no positive eigenvalues with the prescribed constraint of positive fractional Burgers vectors. E_{tot} is composed of: (i) the individual line energies of the four partials: E_{line} , (ii) the interaction of the long-range elastic fields of these four partials: E_{int} , (iii) the misfit energies introduced due to the presence of NNAPB and NNNAPB faults: E_{mis} and (iv) the work done by the external stress field W .

$$E_{tot} = E_{line} + E_{int} + E_{mis} - W \quad (4)$$

The E_{line} term can be expressed as the sum of the individual line energies of four $a/4 \langle 111 \rangle$ partials as follows:

$$E_{line} = E_{line,1} + E_{line,2} + E_{line,3} + E_{line,4} = E_{line,1} + \frac{3K_s b^2}{4\pi} \ln\left(\frac{R}{\xi}\right) \quad (5)$$

The variables R and ξ represent the outer cut-off and inner-cut off distances which are chosen as $500 b$ and half of the interplanar spacing, a' , across $\langle 111 \rangle$ direction-complying with the original Peierls–Nabarro analysis,respectively. The slip initiation along $\langle 111 \rangle \{110\}$ or $\langle 111 \rangle \{112\}$ systems is associated with the glide of the leading partial; therefore, its individual line energy, $E_{line,1}$, is detailed in a fashion including the short-range energy contribution of the fractional dislocations composing the leading partial dislocation.

The long range interaction energy of the $a/4 \langle 111 \rangle$ partials with each other, E_{int} , is expressed in Eq. (6) where p represents the number of the total partials, i.e. 4, and the separation distance between the third and fourth partials (the leading partial is denoted as the first partial),i.e. d_3 , is taken as equal to d_1 as shown in Fig. 2 (Wang and Sehitoglu, 2014):

$$E_{int} = \frac{K_s b^2}{4\pi} \left\{ \sum_{i=1}^{p-1} \left[\sum_{j=1}^i \ln\left(\frac{R}{d_j}\right) + \sum_{j=2}^i \ln\left(\frac{R}{d_j}\right) + \sum_{j=3}^i \ln\left(\frac{R}{d_j}\right) \right] \right\} \quad (6)$$

The misfit energy created on the glide plane via creating stable NNABP and NNNAPB fault ribbons spanning d_1 and d_2 distances in the dissociated configuration of a $\langle 111 \rangle$ dislocation, E_{mis} is formulated as (2NNAPB and 1 NNNAPB type faults):

$$E_{mis} = 2\gamma_1 d_1 + \gamma_2 d_2 \quad (7)$$

Lastly, the energy contribution of the work done by the external stress, W , on the leading partial dislocation configuration is expressed in Eq. (8) as:

$$W = b_1 \tau_1 + b_2 \tau_2 + b_3 \tau_3 \quad (8)$$

where $\{\tau_1, \tau_2, \tau_3\} = \{\Sigma_{23}, \Sigma_{23} \cos \omega - \Sigma_{13} \sin \omega, \Sigma_{23} \cos \alpha + \Sigma_{13} \sin \alpha\}$ following the coordinate transformation operations. It should be emphasized that as the CRSS level is determined based on the glide motion of the leading partial; the trailing partials do not contribute to the work expression in Eq. (8). The resolved components $\{\tau_1, \tau_2, \tau_3\}$ are illustrated in Fig. 5 along with the non-planar structure of the leading partial core. It is to be noted that the conjugate plane angles, α and ω , are determined based on the geometry of the possible four core configurations A, B, C and D shown in Fig. 2.

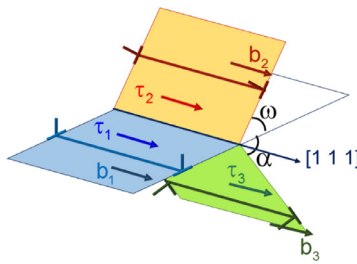


Fig. 5. Shows the geometry of the leading partial core and the resolved shear stresses τ_1 , τ_2 and τ_3 acting on the core fractionals.

201 $E_{line,1}$, is expressed in Eq. (9) as a combination of: (i) the line energies of the fractional dislocations posited inside the
202 core, $E_{fractional}$, (ii) the interaction energies of these fractional dislocations, $E_{inter-fractional}$, (iii) the misfit energy associated with
203 the generalized stacking faults formed on the conjugate {112} and/or {110} planes: E_{fault} . It should be emphasized that the
204 values of these energy terms are governed by the splitting configuration favored upon the minimization of E_{tot} .

$$E_{line,1} = E_{fractional} + E_{inter-fractional} + E_{fault} = \sum_{j=1}^3 E_{fractional,j} + E_{inter-fractional} + E_{fault} \quad (9)$$

205 The term $E_{fractional}$ is comprised of the summation of the line energies associated with three fractional dislocations inside
206 the leading partial and it is expressed as:

$$E_{fractional} = \sum_{i=1}^3 E_{fractional,i} = \frac{K_s}{4\pi} (b_1^2 + b_2^2 + b_3^2) \ln\left(\frac{R}{\xi}\right) \quad (10)$$

207 ensuring the conservation of the Burgers vector of the leading partial as expressed in Eq. (11):

$$\sum_{i=1}^3 b_i = b = |a/4 < 111 >| \quad (11)$$

208 On the other hand, the interaction energy associated with the interplay of the elastic fields of these three core fractional
209 dislocations are expressed as (Lejček and Kroupa, 1981):

$$E_{inter-fractional} = \frac{K_{interaction}}{4\pi} \left(b_1 b_2 \ln\left[\frac{R^2}{y_1^2 + y_2^2 + y_1 y_2}\right] + b_1 b_3 \ln\left[\frac{R^2}{y_1^2 + y_3^2 + y_1 y_3}\right] + b_2 b_3 \ln\left[\frac{R^2}{y_2^2 + y_3^2 + y_2 y_3}\right] \right) \quad (12)$$

210 A major point to emphasize is that the anisotropic elastic interaction coefficient $K_{interaction} = 86.9$ GPa appearing in
211 Eq. (12) is slightly different from $K_s = 84$ GPa as the glide planes of the interacting fractional dislocations are not neces-
212 sarily parallel and may exhibit different crystallographic symmetries along the directions normal to glide direction (111)
213 (Steeds, 1973; Lothe, 1992; Foreman, 1955) (The principal elastic stiffness tensor values of $C_{11} = 116$ GPa, $C_{12} = 102$ GPa and
214 $C_{44} = 84$ GPa (in Voigt notation) are employed).

215 In order to determine the misfit energy of the stacking faults inside the leading partial core separating the fractional
216 dislocations, we need to introduce the mathematical expressions for the disregistry functions $f_i(x_i)$ on the conjugate planes.
217 The functions $f_i(x_i)$ are the generalized forms of the u_x parameter in Fig. 1 which account for the spatial variation of the
218 slip in defects particularly the localization effects in dislocations, and allow us to relate the GSFE value to the spatial
219 coordinates x_i such that $\gamma(u_x) = \gamma(f_i(x_i))$. The non-planar disregistry distribution within the core region of the leading
220 partial is described based on a general form initially proposed by Foreman et al. (1951) and Kroupa and Lejček (1972) which
221 is expressed in Eq. (13).

$$f_i(x_i) = b_i + c_i \xi \left(\tan^{-1}\left(\frac{y_i - x_i}{\xi}\right) - \tan^{-1}\left(\frac{y_i}{\xi}\right) \right) (i = 1, 2, 3) \quad (13)$$

222 The parameters c_i are determined by the set of boundary conditions expressed in Eqs. (14) and (15). Among these two
223 expressions, Eq. (14) indicates that the value of the disregistry functions $f_i(x_i)$ correspond to the fractional Burgers vectors,
224 b_i , at the dislocation line position $x_i = 0$. On the other hand, Eq. (15) implies that the localized slip present at the core center
225 attenuates at far-field as $x_i \rightarrow \infty$.

$$f_i(0) = b_i \quad (14)$$

$$\lim_{x_i \rightarrow \infty} f_i(x_i) = 0 (i = 1, 2, 3) \quad (15)$$

227 By solving Eqs. (14) and (15) simultaneously, the c_i parameters are evaluated to be as:

$$c_i = \frac{b_i}{\xi \left[\tan^{-1}\left(\frac{y_i}{\xi}\right) + \frac{\pi}{2} \right]} \quad (16)$$

Following the introduction of the disregistry function formalism, the misfit energy inside the leading partial core, E_{fault} , is expressed in a convergent serial form presented in Eq. (17) (Lothe, 1992; Tadmor and Miller, 2011):

$$E_{fault} = \sum_{i=1}^3 \sum_{m=\infty}^{\infty} \gamma_i(f_i(ma' - y_i))a' \quad (17)$$

In the expression of E_{fault} , the first summation on the right hand side is taken over the three conjugate planes on which the dislocation core spreads whereas the second sum represents the collection of the fault energy along each atomic row separated by a distance of a' . To that end, Eq. (17) accounts for the discrete structure of the lattice by expressing x_i coordinate as $ma' - y_i$. The equilibrium of the four a/4 ⟨111⟩ partials under either zero or finite external stress necessitates the minimization of the total energy expression given in Eq. (4) which is detailed through Eqs. (5)–(17). This implies the determination of the Burgers vectors, i.e. b_1 , b_2 (b_3 is given as $b_3 = b - b_1 - b_2$) and the positions of the fractionals, i.e. y_1 , y_2 and y_3 , inside the core region of the leading partial.

237 2.4. Solution strategy

To solve for the positions of the fractionals $\{y_1, y_2, y_3\}$ and the Burgers vectors $\{b_1, b_2, b_3\}$, we minimized E_{tot} : $E_{tot}(y_1, y_2, y_3, b_1, b_2, b_3)$ via ensuring the equilibrium of fractional dislocations is ensured. The set of three equations which impose the equilibrium of the i^{th} fractional dislocation under external stress is written in Eq. (18) as follows:

$$\frac{\partial E_{tot}}{\partial y_i} = 0 \quad (i = 1, 2, 3) \quad (18)$$

Furthermore, the constraint presented in Eq. (11) imposes that the summation of the fractional Burgers vector should result into the leading partial Burgers vector, b , and results in 3 additional equations with an unknown Lagrange multiplier μ such that:

$$\nabla_{b_i} E_{tot} + \mu \nabla_{b_i} \left(\sum_{i=1}^3 b_i \right) = 0 \quad (19)$$

In Eq. (19), $\nabla_{b_i}()$ is the gradient operator with respect to the fractional Burgers vector b_i . Given the set of 7 equations in Eq. (11) and Eqs. (18)–(19), the set of 7 unknowns of $\{y_1, y_2, y_3, b_1, b_2, b_3, \mu\}$ are solved numerically.

The expression of E_{tot} is denoted as "stable" up until the inactive constraints can be ensured in response to the proportional increase of Σ components. On the other hand, incremental loading physically tends to drive Burgers vectors of the fractional dislocations b_2 and b_3 into the unphysical negative sign domain and results in ill-conditioning (Fletcher, 2013). Therefore, the maximum value of glide stress Σ_{23} at which the presence of the local minimum of E_{tot} is ensured under the prescribed constraint corresponds to the CRSS level.

The solution strategy adopted herein differs from the minimization of the total energy functional proposed earlier for calculating the core configuration of a/2 ⟨111⟩ dislocations in pure bcc metals (Vitek et al., 1972; Lejček, 1979). In that earlier approach, $\rho_i(x_i)$ distributions on the conjugate planes are evaluated based on the integro-differential Peierls-Nabarro equation. In this work, the fractional dislocation concept is employed to transform the problem of energy functional minimization into a constrained minimization problem of differential calculus. The underlying reason for constructing a different strategy is that the interaction of the disregistry distributions on the conjugate planes introduces an irregular singularity. Unlike the weakly singular integral equations of which are known to be solved by iterative singular value decomposition techniques (Polyanin and Manzhirov, 2008), the existence of solutions for the non-linear, irregularly singular integro-differential equations within the presence of external stress tensor components is not guaranteed (Lejček, 1973). To that end, constraint minimization of E_{tot} is employed within the framework of the set of equations expressed in Eqs. (4)–(19).

261 3. Results

262 3.1. A brief summary of the experimental results on CRSS in single crystals

The confluent effect of non-zero Σ tensor components on the dislocation glide resistance under uniaxial tensile and compression is presented in Fig. 6(a) from the experimental findings of Romero et al. at 323 K (Romero et al., 1988). The glide resistance, CRSS, is quantified based on the critical value of Σ_{23} component. In order to configure the sample orientation and the uniaxial loading sense (either tensile or compressive) effects, the characteristic angle χ of the maximum resolved shear stress plane (MRSSP) is utilized as shown in Fig. 6(b). In this representation convention, the angle χ formed between MRSSP (the plane bearing highest resolved shear stress) and the {110} plane bearing the highest shear stress within the active ⟨111⟩ slip zone, varies between -30° and $+30^\circ$. It is to be emphasized that there is no geometrical restriction on MRSSP and it may coincide with any plane including the reference {110} plane. The sign of the angle χ is taken as positive (negative) if the closest {112} plane to the MRSSP in the active ⟨111⟩ slip zone is sheared along the anti-twinning (twinning) direction under tensile (compression) loading. This representation technique allows us to discern the single crystal orientation under uniaxial loading (Duesbery, 1984).

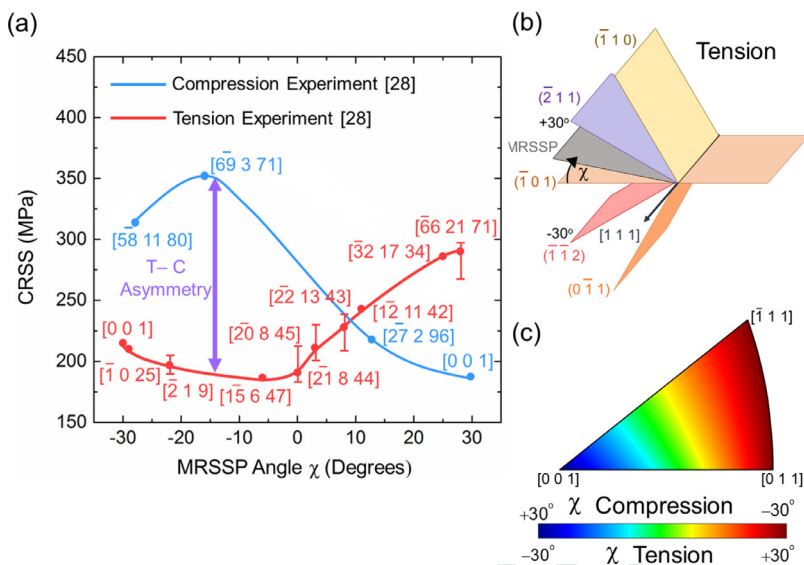


Fig. 6. (a) Shows the variation of the experimental CRSS values under uniaxial tension and compression at 323 K (Romero et al., 1988). It is to be noted that the abbreviation of "T-C" stands for "tension-compression". (b) illustrates the geometrical interpretation of χ angle for uniaxial tension. (c) shows the variation of χ angle on the stereographic triangle for $\{111\}$ slip direction under uniaxial tension and compression respectively. It is to be noted that in the convention employed, the χ value is positive towards the uniaxial tension (compression) orientations favoring the shear along $\{111\}$ $\{112\}$ systems with in the active glide zone in anti-twinning (twinning) sense.

As can be seen in Fig. 6(a), the experimental CRSS levels do not correspond to a unique value and show significant variation ranging from 180 MPa up to 355 MPa under uniaxial tension and compression in response to the different single crystal orientations (Romero et al., 1988). The CRSS levels shown in Fig. 6 exhibit significant deviations from the Schmid Law reaching 95% relative difference between the different uniaxial loading orientations. This difference is fairly large and must be incorporated in any modelling efforts addressing the significant interplay between the core shape and the external stress tensor components.

Under tension, for $\chi \leq 0^\circ$, the glide is favored along the twinning sense on $\{112\}$ glide planes as tabulated in Appendix A (Romero et al., 1988). On the other hand, slip traces are reported to coincide with the MRSSP and $\{123\}$ planes following a wavy glide pattern for single crystal orientations with $\chi > 0^\circ$ (Romero et al., 1988). The promotion of high index slip plane traces for the tensile orientations of $\chi > 0^\circ$ is expected to be a consequence of the segmented slip of screw dislocations along the $\{112\}$ and/or $\{110\}$ planes which have been also observed to incur in other bcc lattice structures such as in pure W (Marichal et al., 2013), Fe (Franciosi et al., 2015) and Fe-Si alloys (Šesták and Zárubová, 1965). On the other hand, this core fractional cross-glide phenomenon is not peculiar to the bcc-derivative lattices. A similar core transformation has been also imaged in a TEM study for the screw dislocations gliding on the prismatic and pyramidal planes intermittently in hcp structured Ti as a result of lattice friction differences in between these two planes (Clouet et al., 2015). In CuZnAl, the segmented, wavy glide for the tensile orientations of $\chi > 0^\circ$ is expected to stem from the fact that the dislocations which are promoted to glide along the anti-twinning sense on $\{112\}$ planes under external stress transform into a glissile configuration which is prone to slip along $\{111\}$ $\{110\}$ and $\{111\}$ $\{112\}$ twinning sense systems. The GSFE profile of $\{111\}$ $\{112\}$ anti-twinning glide system shown in Fig. 1 is expected to play a key role in this anomalous slip behavior.

For the single crystal orientations of $\chi > 0^\circ$ under compression, slip initiates along the twinning sense of the $\{111\}$ $\{112\}$ systems and the high index slip planes are observed for the orientations of $\chi < 0^\circ$. The greatest CRSS differential between the uniaxial tension and the compression is observed within the range of $\chi \in (-20^\circ, -10^\circ)$ and the tension-compression asymmetry vanishes within the close neighborhood of $\chi \approx 10^\circ$. As the change in the sign of χ angle implies nothing but changing the sign of Σ components, this asymmetry in the CRSS values is surmised to be closely related to the different sessile to glissile transformation paths of the dislocation cores under external stress.

3.2. Sessile splitting of $a/4 \langle 111 \rangle$ leading partial core fractionals

The equilibrium core configuration of the screw character leading partial, $a/4 \langle 111 \rangle$, in the absence of an external stress field is of significant importance as it constitutes an initial condition for the core shape evolution under external stress. To that end, we chose the four possible sessile core configurations shown in Fig. 2 in which the core fractionals split on different planes. Thereafter, E_{tot} is minimized to calculate the equilibrium configurations of the fractionals. Table 2, shows the corresponding Burgers vectors and the positions of the fractionals as well as E_{tot} values for each configuration shown in Fig. 7(a), (b), (c) and (d). As Table 2 and Fig. 7 suggest, the $\{112\}$ planes sheared along the twinning sense in the $\{111\}$

Table 2

Tabulation of the maximum values of the disregistry distributions of $f_i(x_i)$ ($i = 1, 2, 3$), namely the Burgers vector of each fractional split on either {110} or {112} conjugate planes, i.e. b_i , inside the core region of the leading $a/4$ [111] partial as well as the fractional positions, y_i , and the total energy values.

	Configuration A	Configuration B	Configuration C	Configuration D
b_1	0.62 b	0.38 b	0.44 b	0.52 b
b_2	0.13 b	0.31 b	0.24 b	0.18 b
b_3	0.25 b	0.31 b	0.32 b	0.30 b
y_1	1.56 b	1.20 b	1.38 b	1.22 b
y_2	0.60 b	1.05 b	0.98 b	0.84 b
y_3	0.25 b	1.05 b	1.16 b	1.06 b
E_{tot} (nJ/m)	12.74	13.56	13.19	12.97

Table 3

Tabulation of the coefficients generating the generalized yield surface plotted in Fig. 11, i.e. τ_{cr} , a_1 , a_2 , a_3 and a_4 . The coefficients are evaluated based on multi-variable regression of the theoretical deviatoric stress components at the instant of glide initiation at which $\Sigma_{23} = S_{23} = \text{CRSS}$.

τ_{cr}	a_1	a_2	a_3	a_4
260	0.85	0.71	0.56	0.25

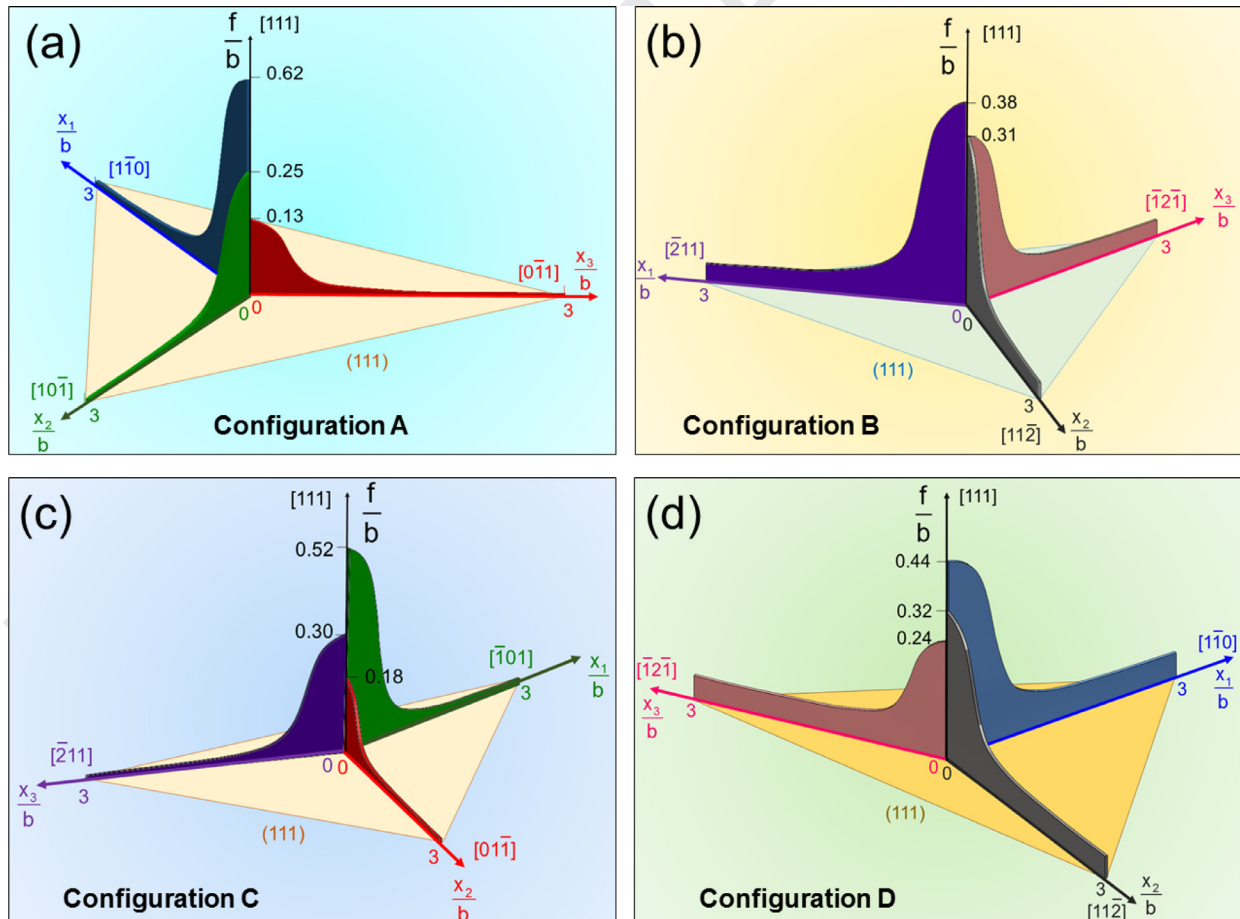


Fig. 7. Shows the sessile, externally stress-free core configurations which are grouped into four categories based on the number and the type of planes on which the fractionals are posited. (a) shows the leading core configuration split on only {112} planes, i.e. configuration A. (b) illustrates the sessile core split on {110} planes only, i.e. configuration B. (c) exhibits the core configuration in which fractionals split on two {112} planes and a single {110} plane, configuration C. In (d), the core fractionals prefer to split on a single {112} plane and two {110} planes, i.e. configuration D.

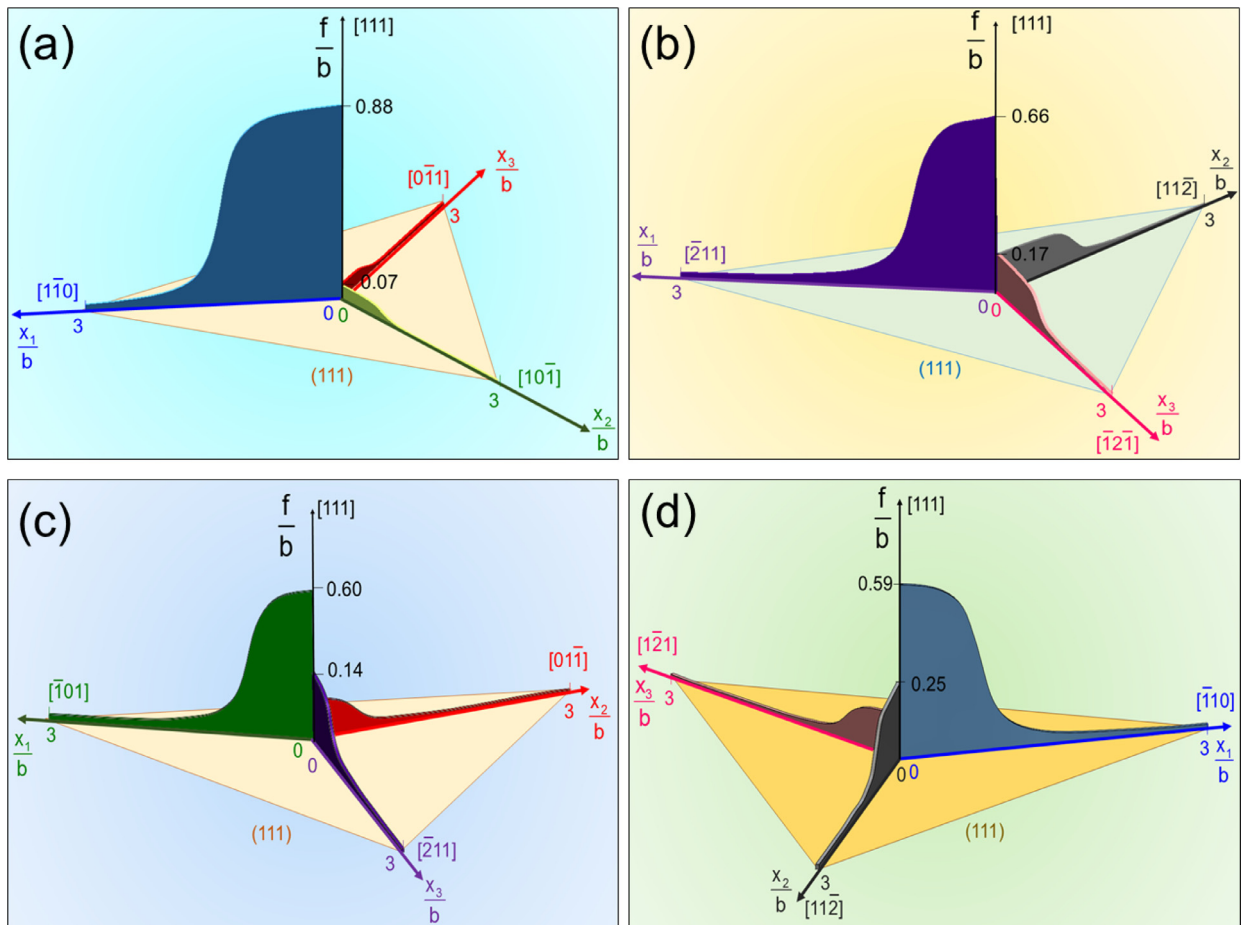


Fig. 8. Shows the theoretical variation of the disregistry distributions inside the non-planar core structure of a/4 [111] screw dislocation posited in a uniaxial tension specimen of $E_1-E_2-E_3 = [5\ 8\ 0]-[0\ 0\ 1]-[850]$ orientation. (a)–(d) shows the disregistry distributions evaluated based on the initial core configurations of A–B–C–D in Fig. 3. As can be seen the greatest disregistry distribution is observed for the configuration A on $(\bar{1}12)[111]$ glide system complying with the experimentally reported active slip system (Romero et al., 1988).

glide zone are energetically more favorable to bear greater Burgers vector in externally stress-free, sessile configuration. This behavior stems from the lower energy of the generalized stacking faults shearing these glide systems. Even though the slip geometries differ significantly for configurations A, B, C and D; only small variations are associated with the E_{tot} levels in the stress free configuration. Therefore, the external stress tensor can introduce transitions between the possible four configurations and hence can affect the resulting CRSS levels. This result necessitates a detailed consideration of the activation of all four configurations under external stress to accurately determine the corresponding CRSS levels.

3.3. The selective activation of configurations under uniaxial loading

In order to build an understanding on the effects of the loading orientation for the sessile to glissile core transformation, we evaluated the slip disregistry distribution of the leading a/4 [111] screw core for a sample oriented as $E_1 - E_2 - E_3$ parallel to $[5\ 8\ 0] - [0\ 0\ 1] - [8\ \bar{5}\ 0]$ triplet under uniaxial tensile loading parallel to E_2 . Among the four possible configurations A, B, C and D shown in Fig. 2; the configuration A reaches the glissile shape earliest- at the lowest resolved shear stress magnitude, i.e. CRSS. The disregistry distribution inside these four core configurations at the instant of the glide initiation is shown in Fig. 8. As can be seen, complying with the fact that the core configuration A attains the glissile shape at the lowest CRSS level, the peak value of the normalized disregistry distribution on $(\bar{1}12)[111]$ glide system, 0.88, is the greatest one among the other configurations (B, C and D), i.e. 0.66, 0.59 and 0.60 respectively. This result suggests that the re-distribution of disregistry inside the core under external stress may play a decisive role in the glide tendency of the leading partial. Furthermore, this trend in the glide resistance of the different configurations also complies with the experimentally observed glide behavior of the [001] tension sample in which the observed glide system is tabulated in Table A.2 (Romero et al., 1988).

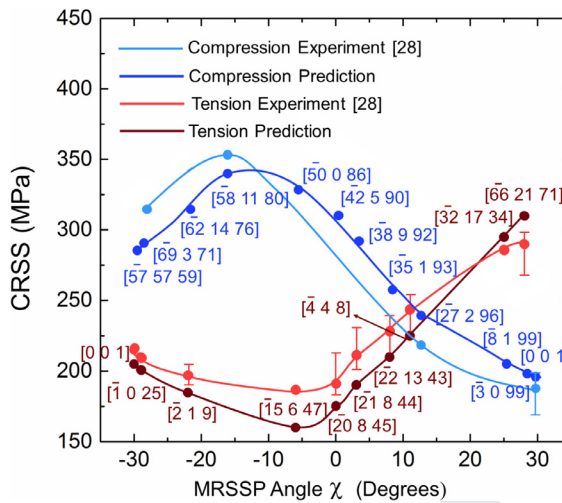


Fig. 9. Shows the theoretical CRSS values within range of $\chi = -30^\circ$ and $+30^\circ$ under uniaxial tension and compression. The experimental CRSS measurements of Romero et al. (1988) (at 323 K) are also included for comparison purposes.

This quantitative analysis suggests that the tendency of the non-planar screw core to attain a glissile shape should be assessed with the transferability of the slip to a favorable glide system from the other conjugate planes that the core extends on. The transfer of slip inside the core region casts the core in a nearly planar shape decreasing the CRSS level. This attitude in the core structure complies with the original Peierls-Nabarro model suggesting a lower glide resistance for a wider planar core (Lothe, 1982). Quantitative evidence between the glide tendency and the planarity of the core structure has been also observed for NiTi within the framework of atomistic scale simulations in our previous work (Alkan and Sehitoglu, 2017). The active configurations simulated for the other loading orientations are also tabulated in Appendix A. The variation of the core planarity and the active core configuration under varying uniaxial loading orientation suggests that the external stress tensor governs on the core splitting geometry; and therefore, on the CRSS level. This correspondence between the core shape and the CRSS level will be detailed in the following section.

3.4. Theoretical predictions of CRSS under uniaxial tension and compression

Following the formulation introduced in Sections 2.3 and 2.4, we evaluated the theoretical critical glide stress values, i.e. theoretical CRSS, and plotted them in Fig. 9 in comparison with the uniaxial tension and compression experiments of Romero et al. (1988). As can be seen, the theoretical predictions can capture the trend observed in the experimental measurements in a reasonably well agreement. This close trend between the theory and the experiments allows us to deduce the possible underlying mechanisms for the non-Schmid behavior in CRSS values of CuZnAl. Tension-compression asymmetry shown in Fig. 9 exhibits strong anisotropy. Meanwhile, the CRSS differentials extend up to 175 MPa for the set of orientations $\chi \in (-15^\circ, -5^\circ)$, it almost vanishes for $\chi \in (10^\circ, 15^\circ)$ interval. Activation of the distinct slip systems in these crystallographic orientations provides evidence for the presence of a direct link with the core shape and the corresponding CRSS levels. In order to shed light on the interplay between the core shape and the CRSS levels, we plotted the theoretical distribution of core disregistry displacements for the $[58 11 80]$ compression, the $[15 6 47]$ tension, the $[27 2 96]$ compression and the $[4 4 8]$ tension samples respectively in Fig. 10(a)–(d) at the instant of $\Sigma_{23} = \text{CRSS}$.

A close examination of Fig. 10(a) and (b) demonstrates that the planarity of the disregistry distribution inside the leading partial core spreading plays a key role in the major CRSS differential plotted in Fig. 9 between the $[58 11 80]$ compression and the $[15 6 47]$ tension samples. The core shape preserves its non-planarity for the $[58 11 80]$ compression sample as the glide shear stress reaches the CRSS value, as shown in Fig. 10(a). On the contrary, the planarity of the core structure can be clearly observed in the $[15 6 47]$ tension sample in which the core disregistry is concentrated mostly on the $(\bar{1}\bar{1}2)$ glide plane, with a Burgers vector of $b_1 = 0.94$ b in Fig. 10(b). These theoretical disregistry distributions suggest that the planar core structures can decrease the corresponding CRSS levels compared to the non-planar core spreading. This core planarity effect is evaluated to result in strong anisotropy in the glide resistance of CuZnAl depending on the sample orientation.

But not all of the sample orientations suffer from the strong CRSS asymmetry between the uniaxial tension and compression. As can be seen in Fig. 9, within the range of χ values of $(10^\circ, 15^\circ)$, the gap between the CRSS values are almost indistinguishable. On theoretical grounds, this behavior stems from the very similar core shape attained under external stress as exemplified for the $[4 4 8]$ tension and the $[27 2 96]$ compression samples as shown in Fig. 10(c) and (d) at the instant of $\Sigma_{23} = \text{CRSS}$. The minor differences in these two core spreading cases are surmised to stem from the distinct GSFE profiles of the $\langle 111 \rangle \{110\}$ and $\langle 111 \rangle \{112\}$ systems.

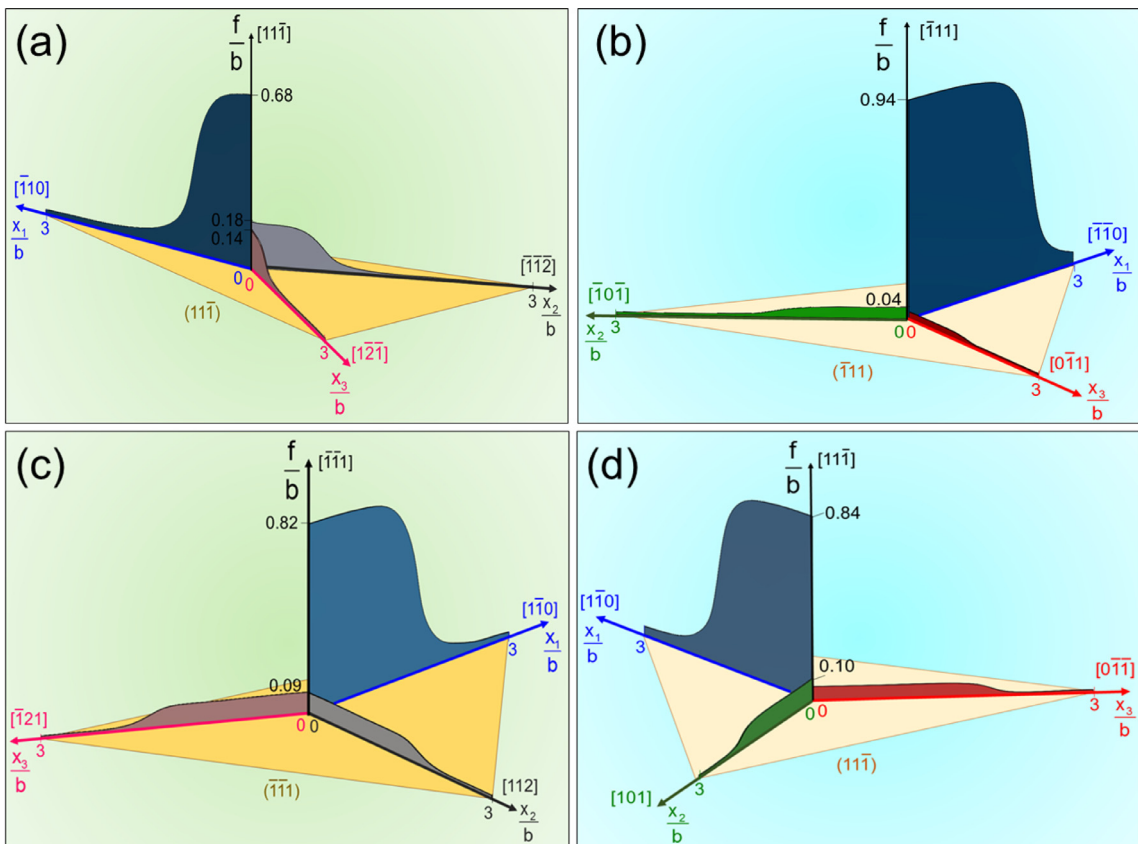


Fig. 10. (a) shows the disregistry distribution inside the leading partial core evaluated for the [581180] sample under uniaxial compression at the instant of glide initiation. Similarly, (b) shows the disregistry distribution evaluated for the [15647] sample under uniaxial tension. As can be seen by comparing the core configurations shown in (a) and (b), the transferability of the non-planar disregistry distribution into a planar shape is of paramount importance governing on the experimental and the theoretical CRSS values plotted in Fig. 9. The non-planar core shape of the leading partial posited in the [581180] compression sample introduces an increase of 175 MPa in the CRSS level compared to the [15647] tension sample which is in line with the experimental 165 MPa difference. On the other hand, the CRSS values are very close, by only 10 MPa, for the [448] tension and the [27296] compression samples of which the core disregistry distributions at the instant of glide initiation are plotted in (c) and (d), respectively. As can be seen in (c) and (d), the disregistry distributions are very similar for both samples. The underlying reason for the minor difference in CRSS levels can attributed to the GSFE profiles of $\{111\}$ {110} and $\{111\}$ {112} planes which contribute to E_{tot} as manifested in a detailed fashion in *Methods and Theoretical Background* section.

These illustrative cases clearly suggest that the promoted core configuration and the corresponding disregistry profiles are in close relationship with the CRSS values measured/calculated. The planarity of the core structure facilitates glide motion and plays a key role in the anisotropic behavior of CRSS levels. The instability of the E_{tot} expression to pinpoint the glide initiation is shown to result in close agreement with the experimental behavior in CuZnAl. On the other hand, this method requires a case by case examination and should be further extended into an applicative form to be employed in continuum scale crystal plasticity calculations. In the following section, this point will be addressed with a proposed generalized yield criterion.

3.5. Construction of a yield surface for the generalized stress states

Following the theoretical efforts in modelling the anisotropic glide behavior of CuZnAl in the previous sections; we established a compact, analytical yield criterion as a function of the theoretical external stress tensor components at the instant of plastic flow. Broadly speaking, this approach allows to generate a closed form expression serving as a quantitative tool for identifying the slip initiation in CuZnAl alloy within the framework of a macroscale crystal plasticity perspective. To accomplish this task, we incorporated the independent deviatoric stress tensor components S_{ij} ($i,j=1,2,3$) which are defined as $S_{ij} = \Sigma_{ij} - 1/3 \text{trace}(\Sigma)\delta_{ij}$ (δ_{ij} : Kronecker Delta), into a linear expression presented in Eq. (20). The coefficients τ_{cr} and a_i ($i=1,2,3,4$) are evaluated by multi-linear regression of the theoretical deviatoric stress components from the energy minimization calculations at the instant of plastic slip initiation such that $S_{23} = \text{CRSS}$. The resulting yield surface is plotted in Fig. 11.

$$\tau_{cr} = S_{23} + a_1 S_{21} + a_2 S_{11} + a_3 S_{22} + a_4 S_{13} \quad (20)$$

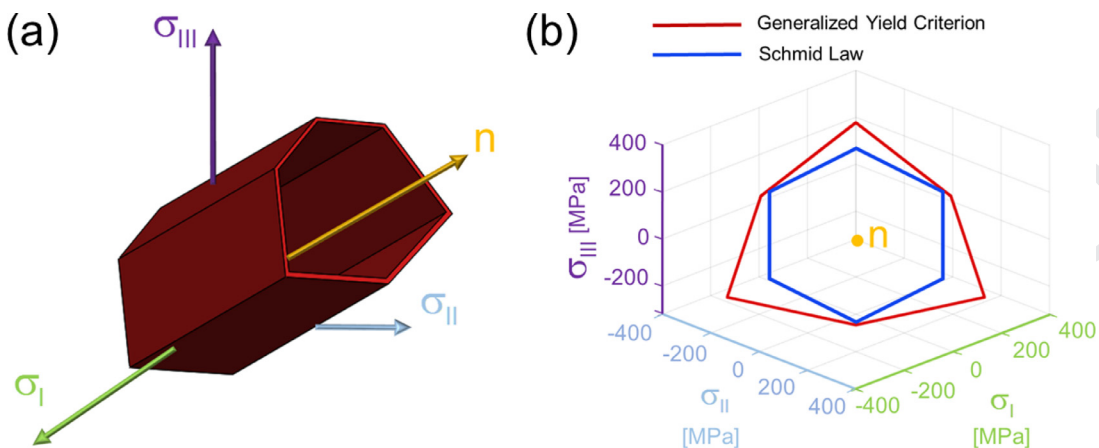


Fig. 11. (a) illustrates the predicted yield hypersurface in the principal stress space. Complying with the previous studies (Alkan et al., 2017; Hill, 1998), the predicted yield surface is of cylindrical topology with a symmetry axis of $n = \Gamma[1, 1, 1]$. (b) shows the yield surface projection on the π plane which is normal to n vector. As can be seen, significant asymmetry is present in the generalized yield surface suggesting the major deviations from the conventional Schmid Law.

378 In order to visualize the resulting effect of the deviatoric stress components other than the glide shear stress Σ_{23} ($= S_{23}$);
 379 the external stress state tensor is expressed in principal stress space of $\sigma_I - \sigma_{II} - \sigma_{III}$ in a diagonalized form. Following
 380 this step, the principal stress components are parameterized utilizing two characteristic angles of θ and ϕ as well as the
 381 proportionality constant λ . In this mathematical representation scheme, θ is the angle between the principal stress vector
 382 $T = [\sigma_I, \sigma_{II}, \sigma_{III}]$ and $\sigma_I = [\sigma_I, 0, 0]$; where as ϕ stands for the angle between projection of $T = [\sigma_I, \sigma_{II}, \sigma_{III}]$ onto the $\sigma_{III} =$
 383 $[0, 0, \sigma_{III}]$ plane and the $\sigma_I = [\sigma_I, 0, 0]$ vector. The magnitude of the proportionality constant λ depends on the minimum
 384 resolved glide shear stress component acting on the possible glide systems satisfying of the generalized yield criterion given
 385 in Eq. (20).

386 To calculate the CRSS levels and the associated deviatoric stress tensor components, we discretized the definition range
 387 of θ and ϕ , i.e. $\theta = [0, \pi]$ and $\phi = [0, 2\pi]$, into 100 increments. Thereafter, the resulting yield hypersurface is generated in
 388 the principal stress space in Fig. 11(a) along with its projection onto the deviatoric plane - also denoted as π plane- in
 389 Fig. 11(b). It should be noted that $n = \Gamma[1, 1, 1]$ where $\Gamma = 1/3(\sigma_I + \sigma_{II} + \sigma_{III})$.

390 4. Discussions

391 The solution of the total energy function encompassing the dislocation core spreading on {112} and {011} planes has
 392 enabled us to configure the core shapes with the corresponding disregistry functions under external stress without a priori
 393 assumptions. The dislocation configurations that are energetically most favorable were identified on a case by case basis.
 394 This methodology allowed determination of CRSS levels associated with slip in tension and compression. The resulting CRSS
 395 levels plotted as a function of loading orientation exhibit dramatic variations in their magnitudes and show close agree-
 396 ment with the experiments (Romero et al., 1988). The results point to much higher CRSS levels under uniaxial compression
 397 compared to tension that can partly explain the wider superelasticity temperature range observed in compression compared
 398 to tension (Wu et al., 2017). Considering that the transformation stresses are far below 25 MPa (Wu et al., 2017); the CRSS
 399 levels exceeding 180 MPa can result in long term performance as the higher slip resistance is known to improve function-
 400 ality of shape memory alloys (Chowdhury and Sehitoglu, 2017). The overall non-Schmid effects in CuZnAl (CRSS variation
 401 from 180 MPa to 355 MPa) are much higher than the NiTi case pointing to the presence of the strong plastic anisotropy
 402 effects complying with the high Zener anisotropy ratio of 12 (Verlinden et al., 1984). The major deviations from the Schmid
 403 Law may result in high internal stresses and be responsible for the complex constitutive response in these alloys including
 404 hysteresis and the texture effects.

405 Accommodation of plastic deformation is mainly accomplished by the a {111} screw character dislocations on {112} and
 406 {110} glide planes in L2₁ ordered CuZnAl although the presence of quenching induced sessile dislocations on the <001>
 407 {110} system has been also reported (Lovey and Torra, 1999). The evolution of the leading partial core configurations from
 408 a sessile to a glissile shape under external stress are evaluated within the framework of the energetic arguments and the
 409 variation of the core spreading has been demonstrated to play a decisive role in the anisotropic glide resistance of CuZnAl.
 410 The calculated core configurations suggest that core planarity facilitates the glide motion leading to the lower CRSS levels.
 411 Furthermore, the resulting CRSS values are forwarded to establish a generalized yield criterion along with the external
 412 stress tensor components. To that end, the determination of atomistically informed CRSS levels under external stress tensor
 413 presents itself as a prospective quantitative tool for the macroscale crystal plasticity calculations nurturing strong ties with
 414 the core configurations.

415 It is to be noted that the original Peierls-Nabarro treatment has proved itself successful in capturing the anisotropic
 416 trend in CRSS levels. On the other hand, the resulting predictions are usually 3 to 4 times greater in magnitude than the
 417 experimental measurements. In this work, by varying both short and long range energy terms as a function of applied stress
 418 state embracing the non-planar core geometry, CRSS predictions are demonstrated to be in excellent agreement with the
 419 experimental measurements. On the other hand, the contribution of thermally activated mechanisms to CRSS levels at finite
 420 temperatures should be necessarily recognized to assess the limits of the current analysis (Taylor, 1992).

421 The contribution of a $\langle 111 \rangle$ screw dislocations in the plastic deformation of CuZnAl is not limited to the austenitic phase.
 422 CuZnAl can go into thermally/stress-induced thermoelastic martensitic transformation from the austenitic β phase (L_2
 423 ordered) to the martensitic 18R phase (face-centered tetragonal ordered). To that end, the inherited a $\langle 111 \rangle$ dislocations
 424 from the austenite phase can also prevail on the functional behavior of CuZnAl. Following the phenomenological theory
 425 of martensitic transformation (Wechsler et al., 1953; De Vos et al., 1978), it is shown in Appendix C that $\langle 111 \rangle \{110\}$ and
 426 $\langle 111 \rangle \{112\}$ glide directions of austenite phase are inherited as $<120>_{18R}\{22\ 11\ 2\}_{18R}$ and $<120>_{18R}\{211\}_{18R}$ into the 18R
 427 martensite phase. The inherited dislocations in the 18 R phase are not as glissile as they are in the austenitic phase as
 428 shown in Fig. B.2 and discussed in Appendix B regarding the magnitude of the resolved glide stress acting on them. In
 429 response, these inherited defects may introduce internal stresses affecting both forward and the reverse transformation be-
 430 havior [Chowdhury and Sehitoglu, 2016; Romero and Ahlers, 1989; Sade et al., 2007]. The resulting internal stress fields may
 431 widen the hysteresis and increase the critical forward transformation stress stabilizing the austenitic β phase (Lovey and
 432 Torra, 1999). Furthermore, the stress fields around the dislocations may even promote the nucleation of preferential variants.
 433 The core configuration of partial dislocations and the deviations from Schmid Law is of paramount importance in describ-
 434 ing the interplay between the austenitic slip and martensitic transformation. On the other hand, a thorough explanation
 435 of these intricate interaction mechanisms necessitates to build a profound quantitative knowledge regarding the plastic slip
 436 and martensitic transformation mechanisms in CuZnAl. Therefore, this work aims to shed light on the theoretical character-
 437 ization of slip initiation in the austenitic CuZnAl within the framework of slip energetics formulation. In fine, the resulting
 438 CRSS values are shown to exhibit strong deviations from the Schmid Law as a function of the core configurations promoted
 439 under external stress. Theoretical calculations exhibit close agreement with the experimental measurements and pave the
 440 way for establishing a generalized yield criterion for macroscale crystal plasticity modelling efforts.

441 It should be noted that the magnitude of the observed asymmetry between the different single crystal orientations es-
 442 tablishes a motivation to comprehend the functional performance of polycrystalline CuZnAl (Gall et al., 1998). Since drawn
 443 CuZnAl has evidence of crystallographic texture, it is extremely important to understand the anisotropic variations in the
 444 CRSS levels. The current methodologies for describing the flow behavior of the Cu based shape memory alloys are rather
 445 simple, and do not recognize the important role of anisotropic slip resistance in shape memory behavior. To that end, the
 446 resultant generalized yield criterion should assist those researchers who are modeling plasticity of Cu-based shape memory
 447 alloys at the continuum level.

448 5. Conclusions

449 Following conclusions are drawn from this work:

- 450 (1) The orientation dependence of slip stress in CuZnAl is significant and shows a complex trend due to the activation of
 451 $\langle 111 \rangle \{112\}$ and $\langle 111 \rangle \{011\}$ systems depending on the orientation.
- 452 (2) The difference in the generalized stacking fault energy curves of $\{112\}$ plane along the twinning and the anti-twinning
 453 senses can not solely explain the large orientation dependence of the CRSS levels in CuZnAl. Appreciation of the CRSS
 454 levels which deviate from the Schmid Law, necessitates to interrogate the core configurations in detail.
- 455 (3) The results point that the non-planar core structures spread on conjugate $\{112\}$ and $\{011\}$ planes are categorized into four
 456 distinct fractional dislocation combinations which minimizes the overall energy. The calculations utilizing the dislocation
 457 core configurations produce the correct experimental trends in CRSS.
- 458 (4) The results show that the planarity of the disregistry distributions inside the leading partial core plays a significant role
 459 in the magnitude of the CRSS levels. The planar core structures are demonstrated to facilitate the glide motion.
- 460 (5) The proposed generalized yield criterion exhibits significant departure from the Schmid Law, and demonstrates the com-
 461 plexity of the slip anisotropy observed in shape memory alloys.

462 Acknowledgments

463 The work is supported by Nyquist Chair funds.

464 Appendix A

465 The crystallographic orientations of the simulated samples under uniaxial tension and compression are tabulated in
 466 Table A.1 for the uniaxial compression and Table A.2 for the uniaxial tension based on the experimental data reported
 467 for CuZnAl at 323 K in Romero et al. (1988). Furthermore, the active leading partial core configurations calculated within the
 468 framework of E_{tot} expression developed in *Methods and Theoretical Background* are also included.

Table A.1

The characteristic angle χ , the crystallographic directions parallel to the sample frame base vectors E_1-E_2 and the dislocation frame base vectors e_2-e_3 are tabulated for the uniaxial compression loading acting in line with E_2 along with the favored configuration, i.e. either A, B, C or D.

Uniaxial compression			
χ	$E_1 - E_2$	$e_2 - e_3$	Active configuration
-29.7°	[1 1 0]-[575759]	[123]-[11̄1]	D
-28.7°	[1 23 0]-[69371]	[1̄23]-[11̄1]	C
-21.54°	[0387]-[621476]	[1̄23]-[11̄1]	C
-16.26°	[11 58 0]-[581180]	[123]-[11̄1]	D
-6.11°	[43 0 25]-[50086]	[011]-[11̄1]	B
0°	[0181]-[42590]	[1̄21]-[11̄1]	A
3.13°	[3 19 0]-[38692]	[1̄21]-[11̄1]	A
7.61°	[1 35 0]-[35193]	[1̄21]-[11̄1]	A
12.68°	[2 27 0]-[27296]	[1̄21]-[11̄1]	A
25.02°	[1 8 0]-[8199]	[1̄21]-[11̄1]	A
28.3°	[33 0 1]-[3099]	[1̄21]-[11̄1]	A
30°	[0 1 0]-[0 0 1]	[211]-[11̄1]	A

Table A.2

The characteristic angle χ , the crystallographic directions parallel to the sample frame base vectors E_1-E_2 and the dislocation frame base vectors e_2-e_3 are tabulated for the uniaxial tension loading acting in line with E_2 along with the favored configuration, i.e. either A, B, C or D.

Uniaxial tension			
χ	$E_1 - E_2$	$e_2 - e_3$	Active configuration
-30°	[5 8 0]-[0 0 1]	[1̄12]-[1 1 1]	A
-28.6°	[7 3 0]-[1025]	[1 1 2]-[1̄11]	A
-22.43°	[9 1 1]-[219]	[1̄12]-[111]	A
-5.52°	[2 5 0]-[15647]	[1̄12]-[1̄11]	A
-0.15°	[2 5 0]-[20845]	[1̄12]-[1̄11]	A
2.93°	[0112]-[21844]	[011]-[11̄1]	B
7.71°	[04313]-[221343]	[011]-[11̄1]	B
10.89°	[1 1 0]-[448]	[1̄32]-[11̄1]	D
25.12°	[021]-[321734]	[1̄32]-[11̄1]	D
27.81°	[7 22 0]-[662171]	[1̄32]-[11̄1]	D

469 Appendix B

470 To develop a solid understanding for the contribution of the austenitic-inherited slip on the pseudoelastic behavior of
 471 CuZnAl, the crystallographic aspects of the martensitic transformation from L2₁ to 18R crystal structure should be revisited.
 472 To that end, following the generalized crystallographic theory of martensitic transformation of Wechsler et al. (1953) (WLR
 473 theory) from bcc to 18R crystal structures, the glide planes and the directions inherited from the austenite phase into the
 474 martensitic phase are derived.

475 In order to accomplish this task, firstly, the lattice correspondence between the austenitic L2₁ structure (β phase) and
 476 the martensitic 18 R structure (β' phase) is introduced as De Vos et al. (1978) (no subscript is employed for the β phase
 477 indices throughout the text):

$$[100]_{18R}//[100] \quad [010]_{18R}//[011] \quad [001]_{18R}//[0\bar{1}1] \quad (B.1)$$

478 Table B.1 summarizes the lattice parameters of L2₁ and 18 R structures (shown in Fig. B.1) evaluated from the ab-initio
 479 simulations (Wu et al., 2015).

Table B.1

Tabulation of the lattice parameters for L2₁ and 18 R structures evaluated from the ab-initio calculations (Wu et al., 2015).

L2 ₁	18R		
A	a_{18R}	b_{18R}	c_{18R}
5.828 Å	5.26 Å	4.51 Å	38.4 Å

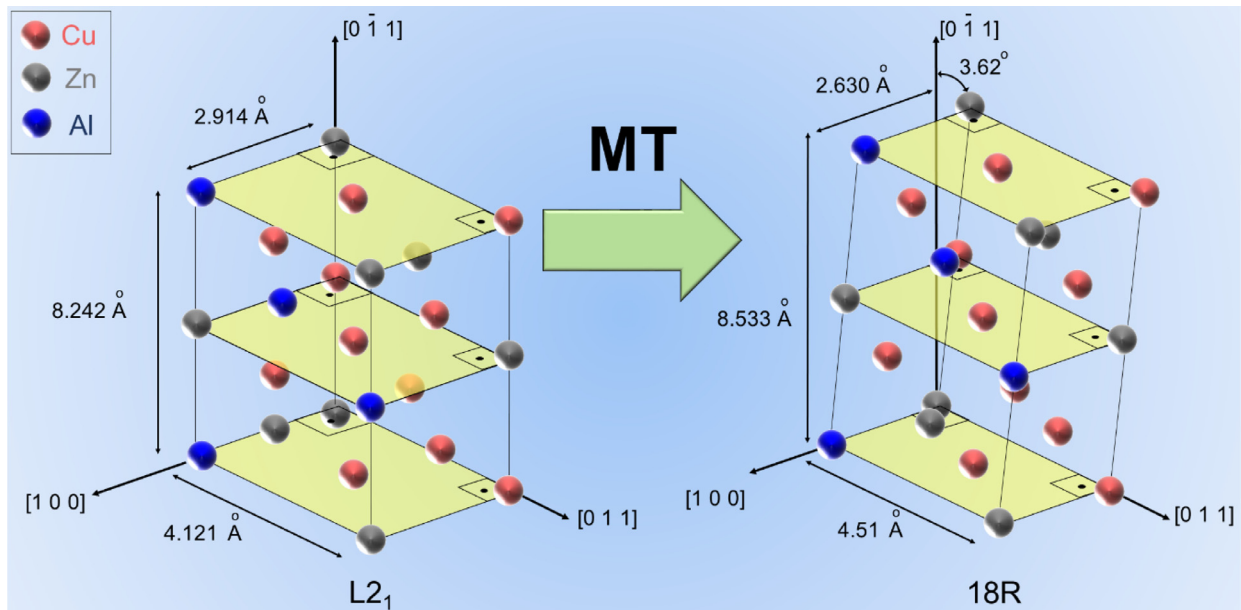


Fig. B.1. This figure illustrates the lattice structures in $L2_1$ ordered austenitic phase and 18 R structured martensite phase under the combined action of M and T deformation tensors.

Table B.2

Tabulation of values of the parameters η_1 , η_2 , η_3 and g, based on the lattice constants and the electron microscopy measurements of de Vos et al. (1978).

η_1	η_2	η_3	g
0.911	1.0681	1.5034	0.1568

480 Thereafter, following the WLR theory, the total deformation gradient tensor, \mathbf{F} , is expressed as in Eq. (B.2):

$$\mathbf{F} = \mathbf{RMT} \quad (\text{B.2})$$

481 where \mathbf{R} , \mathbf{M} and \mathbf{T} are the rotation, the lattice invariant shear and the homogeneous lattice deformation tensors. These
482 tensors are explicitly given as:

$$\mathbf{R} = \frac{1}{\eta_1 + \eta_2 \eta_3} \begin{bmatrix} 1 + \eta_1 \eta_2 \eta_3 & \eta_3 (\eta_1^2 - 1)(\eta_2^2 - 1) & (\eta_3^2 - 1)(1 - \eta_1^2) \\ (1 - \eta_1^2)(\eta_2^2 - 1) & \eta_1 \eta_2 + \eta_3 & (\eta_2^2 - 1)(\eta_3^2 - 1) \\ \eta_2 (\eta_3^2 - 1)(\eta_1^2 - 1) & \eta_1 (1 - \eta_2^2)(\eta_3^2 - 1) & \eta_2 + \eta_1 \eta_3 \end{bmatrix} \quad (\text{B.3})$$

$$\mathbf{M} = \begin{bmatrix} 1 & 0 & 0 \\ 0 & 1 & g \\ 0 & 0 & 1 \end{bmatrix} \quad (\text{B.4})$$

$$\mathbf{T} = \begin{bmatrix} \eta_1 & 0 & 0 \\ 0 & \eta_2 & 0 \\ 0 & 0 & \eta_3 \end{bmatrix} \quad (\text{B.5})$$

483
484
485 With this given structure, \mathbf{F} is an homogeneous deformation tensor and maps vectors into vectors and planes into planes
486 (Wechsler et al., 1953). It is to be noted that there are two existing solutions for the lattice invariant shear, g, appearing
487 Eq. (B.4), within the context of invariant plane deformation, i.e. denoted as g_1 and g_2 (De Vos et al., 1978). These shears are
488 evaluated in terms of, η_2 and η_3 as:

$$g_{1,2} = \pm \frac{1}{\eta_3} \sqrt{(\eta_2 - 1)^2 (\eta_3 - 1)^2} \quad (\text{B.6})$$

489 For demonstration purposes, only the minimum magnitude of these two shears, $g = \min(|g_1|, |g_2|)$, will be employed in
490 the following analysis. On the other hand, it should be emphasized that the conclusions deduced are analogous for both
491 cases on physical grounds. Table B.2 tabulates the values of the parameters η_1 , η_2 , η_3 and g appearing in \mathbf{R} , \mathbf{M} and \mathbf{T} tensors

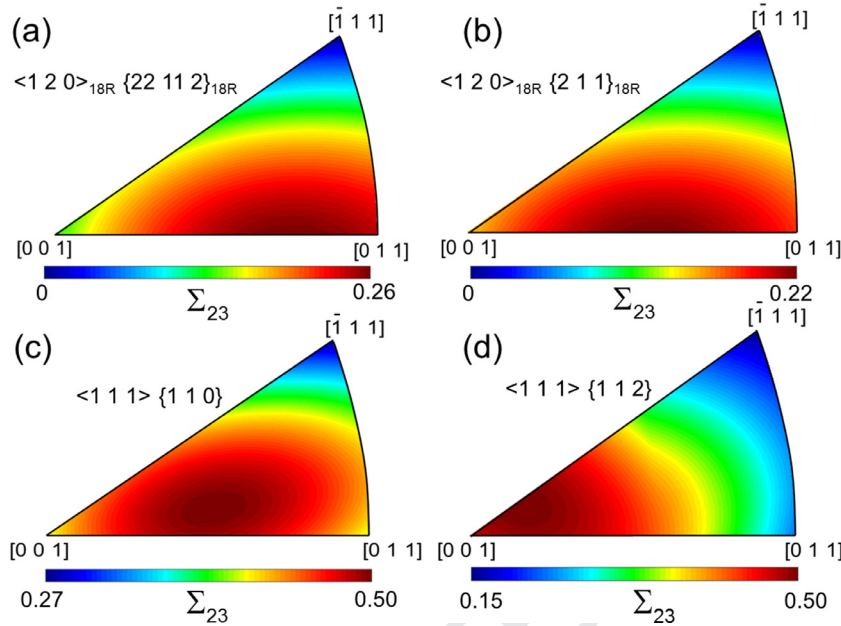


Fig. B.2. Stereographic projection mapping of the glide shear stresses Σ_{23} for the inherited slip systems of (a) $\langle 1\ 2\ 0 \rangle_{18R} \{22\ 11\ -2\}_{18R}$ and (b) $\langle 1\ 2\ 0 \rangle_{18R} \{2\ 1\ 1\}_{18R}$. Similarly, (c) and (d) show the mapping of the parent $\langle 111 \rangle \{110\}$ and $\langle 111 \rangle \{112\}$ systems. As can be seen, the maximum resolved stresses Σ_{23} under unit magnitude uniaxial tensile loading are significantly different between the austenitic and the martensitic phases. Similar analogy can be also established under compression.

492 which are functions of the lattice parameters and the distortions measured in the stacking of the alloying atoms determined
493 via electron microscopy (De Vos et al., 1978).

494 Following the values provided in Table C.2, the deformation gradient tensor \mathbf{F} (for the fundamental variant) is evaluated
495 as:

$$\mathbf{F} = \begin{bmatrix} 0.8927 & -0.0151 & 0.1084 \\ 0.0089 & 1.0520 & -0.3169 \\ -0.0747 & -0.0619 & 1.3980 \end{bmatrix} \quad (\text{B.7})$$

496 Fig. B.1 illustrates the austenitic L₂ and the martensitic 18 R structures for the first 5 stacking layers based on \mathbf{F} tensor.
497 It should be noted that the periodicity in the 18 R structure is captured at the 18th stacking layer normal to $[0\bar{1}\bar{1}]$ direction.

498 Construction of the \mathbf{F} tensor, allows us to establish the correspondence between any vector, \mathbf{m} , in the parent L₂ lattice
499 structure and its inherited vector in the martensitic 18R crystal lattice, \mathbf{m}' , as follows:

$$\mathbf{m}' = \mathbf{F}\mathbf{m} \quad (\text{B.8})$$

500 Similarly, the correspondence between the parent and the inherited planes can be established by operating the defor-
501 mation gradient tensor \mathbf{F} upon the cross product of the two vectors posited on the parent plane. To that end, any vector
502 posited on a specific plane in the parent austenitic phase can be related to its post-transformation direction and plane in
503 the martensitic phase. In particular, $[111](\bar{1}10)$ and $[111](\bar{1}\bar{1}2)$ glide systems in β phase correspond to the following set of
504 glide systems in β' phase:

$$[111](\bar{1}10) \rightarrow [120]_{18R}(\bar{2}\bar{2}\ 11\ \bar{2})_{18R} \quad (\text{B.9})$$

$$[111](\bar{1}\bar{1}2) \rightarrow [120]_{18R}(\bar{2}11)_{18R} \quad (\text{B.10})$$

505 Similar analogy can be also established for the other systems which belong to $\langle 111 \rangle \{112\}$ or $\langle 111 \rangle \{110\}$.

506 Under uniaxial external loading, the determination of the active variant gains significance. The martensitic transformation
507 from L₂ to 18 R structure in CuZnAl alloy consists of 24 variants (De Vos et al., 1978). Considering the correspondence of the
508 slip systems in the austenitic and martensitic phases and the presence of the possible 24 variants; the glide stresses acting
509 along the inherited $[120]_{18R}(\bar{2}\bar{2}\ 11\ \bar{2})_{18R}$ and $[120]_{18R}(\bar{2}11)_{18R}$ systems vary under the uniaxial tension as shown in Fig. B.2.
510 Comparing the resolved glide shear stress Σ_{23} acting on these two inherited systems and the parent $\langle 111 \rangle \{110\}$ and $\langle 111 \rangle \{112\}$ glide systems; it is evident that the inherited a $\langle 111 \rangle$ superlattice dislocations to the martensitic phase are expected
511 to exhibit a sessile behavior as the acting glide forces on the dislocations are considerably smaller in the martensitic phase.
512 Similar analogy can be also established under uniaxial compression.

515 **References**

- 516 Alkan, S., Sehitoglu, H., 2017. Non-Schmid response of Fe3Al: The twin-antitwin slip asymmetry and non-glide shear stress effects. *Acta Materialia* 125,
517 550–566.
- 518 Alkan, S., Sehitoglu, H., 2017. Dislocation core effects on slip response of NiTi- a key to understanding shape memory. *Int. J. Plast.* 97, 126–144.
- 519 Alkan, S., Wu, Y., Sehitoglu, H., 2017. Giant non-schmid effect in NiTi. *Extreme Mech. Lett.* 15, 38–43.
- 520 Basinski, Z.S., Duesbery, M.S., Murty, G.S., 1981. The orientation and temperature dependence of plastic flow in potassium. *Acta Metall.* 29, 801–807.
- 521 Chang, R., 1967. Screw dislocation core structure in body-centred cubic iron. *Philos. Mag.* 16, 1021–1029.
- 522 Chowdhury, P., Sehitoglu, H., 2016. Significance of slip propensity determination in shape memory alloys. *Scripta Materialia* 119, 82–87.
- 523 Chowdhury, P., Sehitoglu, H., 2017. A revisit to atomistic rationale for slip in shape memory alloys. *Prog. Mater. Sci.* 85, 1–42.
- 524 Christian, J., 1983. Some surprising features of the plastic deformation of body-centered cubic metals and alloys. *Metall. Trans. A* 14, 1237–1256.
- 525 Cloet, E., Caillard, D., Chaari, N., Onimus, F., Rodney, D., 2015. Dislocation locking versus easy glide in titanium and zirconium. *Nat. Mater.* 14, 931–936.
- 526 Crawford, R., Ray, I., Cockayne, D., 1973. The weak-beam technique applied to superlattice dislocations in iron-aluminium alloys: II. fourfold dissociation in
527 DO3-type order. *Philos. Mag.* 27, 1–7.
- 528 Dao, M., Asaro, R.J., 1993. Non-Schmid effects and localized plastic flow in intermetallic alloys. *Mater. Sci. Eng.* 170, 143–160.
- 529 De Vos, J.A., Etienne, Delaey, L., 1978. The crystallography of the martensitic transformation of B. C. C. into 9 R: a generalized mathematical model. *Zeitschrift
530 für Metallkunde* 69, 438–444.
- 531 Duesberry, M.S., 1989. The dislocation core and plasticity. In: Nabarro, F.R.N. (Ed.). In: *Dislocations in Solids*, vol. 8, pp. 67–173.
- 532 Duesberry, M., Richardson, G., 1991. The dislocation core in crystalline materials. *Critical Rev. Solid State Mater. Sci.* 17, 1–46.
- 533 Duesberry, M.S., Vitek, V., 1998. Plastic anisotropy in b.c.c. transition metals. *Acta Mater.* 46, 1481–1492.
- 534 Duesberry, M.S., Vitek, V., Bowen, D.K., 1973. The effect of shear stress on the screw dislocation core structure in body-centred cubic lattices. *Proc. R. Soc.
535 London* 332, 85.
- 536 Duesberry, M.S., 1984. On non-glide stresses and their influence on the screw dislocation core in body-centred cubic metals. I. The peierls stress. *Proc. R.
537 Soc. London*. 392, 145.
- 538 Duesberry, M.S., 1984. On non-glide stresses and their influence on the screw dislocation core in body-centred cubic metals II. The core structure, proceedings
539 of the royal society of london, series A. *Math. Phys. Sci.* 392, 175–197.
- 540 Eshelby, J., 1949. LXXXII. Edge dislocations in anisotropic materials. *London Edinburgh Dublin Philos. Mag. J. Sci.* 40, 903–912.
- 541 Fletcher, R., 2013. *Practical Methods of Optimization*. John Wiley & Sons.
- 542 Foreman, A.J., Jaswon, M.A., Wood, J.K., 1951. Factors controlling dislocation widths. *Proc. Phys. Soc. Sec. A* 64, 156.
- 543 Foreman, A.J.E., 1955. Dislocation energies in anisotropic crystals. *Acta Metall.* 3, 322–330.
- 544 Franciosi, P., Le, L.T., Monnet, G., Kahlooun, C., Chavanne, M.H., 2015. Investigation of slip system activity in iron at room temperature by SEM and AFM
545 in-situ tensile and compression tests of iron single crystals. *Int. J. Plast.* 65, 226–249.
- 546 Frederiksen, S.L., Jacobsen, K.W., 2003. Density functional theory studies of screw dislocation core structures in bcc metals. *Philos. Mag.* 83, 365–375.
- 547 Gall, K., Jacobus, K., Sehitoglu, H., Maier, H.J., 1998. Stress-induced martensitic phase transformations in polycrystalline CuZnAl shape memory alloys under
548 different stress states. *Mater. Trans. A* 29, 765–773.
- 549 Gautier, E., Patoor, E., 1997. Experimental Observations for shape memory alloys and transformation induced plasticity phenomena. In: Berveiller, M., Fischer, F.D. (Eds.), *Mechanics of Solids with Phase Changes*. Springer Vienna, Vienna, pp. 69–103.
- 550 Gröger, R., Bailey, A.G., Vitek, V., 2008. Multiscale modeling of plastic deformation of molybdenum and tungsten: I. Atomistic studies of the core structure
551 and glide of 1/2(111) screw dislocations at 0K. *Acta Mater.* 56, 5401–5411.
- 552 Gröger, R., Racherla, V., Bassani, J.L., Vitek, V., 2008. Multiscale modeling of plastic deformation of molybdenum and tungsten: II. Yield criterion for single
553 crystals based on atomistic studies of glide of screw dislocations. *Acta Mater.* 56, 5412–5425.
- 554 Hill, R., 1998. *The Mathematical Theory of Plasticity*. Oxford university press.
- 555 Hirth, J., Lothe, J., 1968. *Theory of Dislocations*. McGraw Hill Book Company.
- 556 Hu, Y.-F., Deng, W., Hao, W.E.N.B., Yue, L., Huang, L., Huang, Y.-Y., Xiong, L.-Y., 2006. Microdefects and electron densities in NiTi shape memory alloys studied
557 by positron annihilation. *Trans. Nonferrous Metals Soc. China* 16, 1259–1262.
- 558 Jara, D.R., Esnouf, C., Guénin, G., 1985. A quantitative study of stable dislocations in the β_1 -phase of Cu-Zn-Al alloys. *Physica Status Solidi (a)* 87, 187–197.
- 559 Kresse, G., Furthmüller, J., 1996. Efficient iterative schemes for ab initio total-energy calculations using a plane-wave basis set. *Phys. Rev. B* 54, 11169–11186.
- 560 Kresse, G., Hafner, J., 1993. Ab initio. *Phys. Rev. B* 48, 13115–13118.
- 561 Kroupa, F., Lejček, L., 1972. Splitting of dislocations in the Peierls-Nabarro model. *Czech. J. Phys. B* 22, 813–825.
- 562 Kroupa, F., Vítek, V., 1967. Slip and the conception of splitting of dislocations in b.c.c. metals. *Can. J. Phys.* 45, 945–971.
- 563 Kroupa, F., Lejček, L., 1981. The effect of shear stress on the screw dislocation core in bcc metals. *Czechoslovak J. Phys.* 31, 719–723.
- 564 Lejček, L., Kroupa, F., 1973. On minimum of energy in the Peierls-Nabarro dislocation model. *Czechoslovak J. Phys.* B 23, 176–178.
- 565 Lejček, L., 1979. Method of an approximate solution of the Peierls-Nabarro equations for non-planar screw dislocation cores. *Czech. J. Phys. B* 29, 196–202.
- 566 Lim, H., Weinberger, C.R., Battaile, C.C., Buchheit, T.E., 2013. Application of generalized non-Schmid yield law to low-temperature plasticity in bcc transition
567 metals. *Model. Simul. Mater. Sci. Eng.* 21, 045015.
- 568 Y.-S. Lin, M. Cak, V. Paidar, V. Vitek, Why is the slip direction different in different B2 alloys?, 2012.
- 569 Lothe, J.P.H.J., 1982. *Theory of Dislocations*, second ed. Krieger Pub. Co..
- 570 Lothe, J.P.H.J., 1992. *Theory of Dislocations*, second ed. Krieger Pub. Co..
- 571 Lovey, F.C., Torra, V., 1999. Shape memory in Cu-based alloys: phenomenological behavior at the mesoscale level and interaction of martensitic transforma-
572 tion with structural defects in Cu-Zn-Al. *Prog. Mater. Sci.* 44, 189–289.
- 573 Marichal, C., Van Swygenhoven, H., Van Petegem, S., Borca, C., 2013. {110} Slip with {112} slip traces in bcc Tungsten. *Sci. Rep.* 3, 2547.
- 574 Otsuka, K., Wayman, C.M. (Eds.), 1998. *Shape Memory Materials*. Cambridge University Press, Cambridge.
- 575 Patra, A., Zhu, T., McDowell, D.L., 2014. Constitutive equations for modeling non-Schmid effects in single crystal bcc-Fe at low and ambient temperatures.
576 Int. J. Plast. 59, 1–14.
- 577 Polyanin, A.D., Manzhirov, A.V., 2008. *Handbook of Integral Equations*. CRC press.
- 578 Qin, Q., Bassani, J.L., 1992. Non-schmid yield behavior in single crystals. *J. Mech. Phys. Solids* 40, 813–833.
- 579 Romero, R., Ahlers, M., 1989. The influence of β -phase plastic deformation on the martensitic transformation in Cu-Zn-Al single crystals. *Philos. Mag. A* 59,
580 1103–1112.
- 581 Romero, R., Lovey, F., Ahlers, M., 1988. Plasticity in β phase Cu-Zn-Al alloys. *Philos. Mag. A* 58, 881–903.
- 582 Sade, M., Uribarri, A., Lovey, F., 1987. An electron-microscopy study of dislocation structures in fatigued Cu-Zn-Al shape-memory alloys. *Philos. Mag. A* 55,
583 445–461.
- 584 Sade, M., Damiani, C., Gastien, R., Lovey, F.C., Malarria, J., Yawny, A., 2007. Fatigue and martensitic transitions in Cu-Zn-Al and Cu-Al-Ni single crystals:
585 mechanical behaviour, defects and diffusive phenomena. *Smart Mater. Struct.* 16, S126.
- 586 Schmid, E., Boas, W., 1950. *Plasticity of Crystals*. A. Hughes and Co., London.
- 587 Šesták, B., Zárubová, N., 1965. Asymmetry of slip in Fe-Si alloy single crystals. *Phys. Status Solidi (b)* 10, 239–250.
- 588 Sherwood, P.J., Guiu, F., Kim, H.C., Pratt, P.L., 1967. Plastic anisotropy of Tantalum, Niobium, and Molybdenum. *Can. J. Phys.* 45, 1075–1089.
- 589 Steeds, J.W., 1973. *Introduction to Anisotropic Elasticity Theory of Dislocations*. Clarendon Press.
- 590 Sutou, Y., Omori, T., Kainuma, R., Ishida, K., 2008. Ductile Cu-Al-Mn based shape memory alloys: general properties and applications. *Mater. Sci. Tech.* 24,
591 896–901.

- 593 Suzuki, H., 1968. Motion of Dislocations in Body-Centered Cubic Crystals. *Dislocation Dynamics* McGraw-Hill USA, pp. 679–700.
- 594 Tadmor, E.B., Miller, R.E., Modeling materials - continuum, atomistic and multiscale technique (2011).
- 595 Taylor, G.I., 1928. The deformation of crystals of β -Brass. *Proc. R. Soc. London. Series A* 118, 1–24.
- 596 Taylor, G., 1992. Thermally-activated deformation of BCC metals and alloys. *Prog. Mater. Sci.* 36, 29–61.
- 597 Vitek, V., Kroupa, F., 1969. Generalized splitting of dislocations. *Philos. Mag.* 19, 265–284.
- 598 Vitek, V., Perrin, R.C., Bowen, D.K., 1970. The core structure of $\frac{1}{2}(111)$ screw dislocations in b.c.c. crystals. *Philos. Mag.* 21, 1049–1073.
- 599 Verlinden, B., Suzuki, T., Delaey, L., Guenin, G., 1984. Third order elastic constants of β Cu-Zn-Al as a function of the temperature. *Scripta Metall.* 18, 600 975–979.
- 601 Vitek V., V. Paidar, Nonplanar dislocation cores: a ubiquitous phenomenon affecting mechanical properties of crystalline materials, 2008.
- 602 Vitek, V., Lejček, L., Bowen, D., 1972. On the factors controlling the structure of dislocation cores in bcc crystals. In: *Interatomic Potentials and Simulation of Lattice Defects*. Springer, pp. 493–508.
- 604 Vitek, V., 1968. Intrinsic stacking faults in body-centred cubic crystals. *Philos. Mag.* 18, 773.
- 605 Vitek, V., 1974. Theory of the core structures of dislocations in body-centred-cubic metals. *Crystal Lattice Defects* 5, 1–34.
- 606 Vitek, V., 1985. Effect of dislocation core structure on the plastic properties of metallic materials. In: *Fiftieth Anniversary of the Concept of Dislocation in Crystals*. The Institute of Metals, London, pp. 30–50.
- 608 Wang, J., Sehitoglu, H., 2014. Dislocation slip and twinning in Ni-based L12 type alloys. *Intermetallics* 52, 20–31.
- 609 Wang, G., Strachan, A., Cagin, T., Goddard, W.A., 2001. Molecular dynamics simulations of $1/2\ a\langle 1\ 1\ 1\rangle$ screw dislocation in Ta. *Mater. Sci. Eng. A* 309, 610 133–137.
- 611 Wayman, C.M., 1980. Some applications of shape-memory alloys. *JOM* 32, 129–137.
- 612 Wechsler, M.S., Lieberman, D.S., Read, T.A., 1953. On theory of formation of martensite. *J. Metals* 5, 1503–1515.
- 613 Woodward, C., Rao, S.I., 2001. Ab-initio simulation of isolated screw dislocations in bcc Mo and Ta. *Philos. Mag. A* 81, 1305–1316.
- 614 Wu, Y., Ojha, A., Patriarca, L., Sehitoglu, H., 2015. Fatigue crack growth fundamentals in shape memory alloys. *Shape Memory Superelast.* 1, 18–40.
- 615 Wu, Y., Ertekin, E., Sehitoglu, H., 2017. Elastocaloric cooling capacity of shape memory alloys – Role of deformation temperatures, mechanical cycling, stress 616 hysteresis and inhomogeneity of transformation. *Acta Mater.* 135, 158–176.
- 617 Wu, M.H., 1990. Cu-based shape memory alloys A2 - Duerig, T.W. In: Melton, K.N., Stöckel, D., Wayman, C.M. (Eds.), *Engineering Aspects of Shape Memory Alloys*. Butterworth-Heinemann, pp. 69–88.
- 619 Yamaguchi, M., Umakoshi, Y., 1983. Dislocations in b.c.c. metals and ordered alloys and compounds with b.c.c.-based ordered structures. In: Paidar, V., 620 Lejcek, L. (Eds.), *The Structure and Properties of Crystal Defects*. Elsevier, Czechoslovakia.